J. Fluid Mech. (2023), *vol*. 954, A23, doi:10.1017/jfm.2022.1011

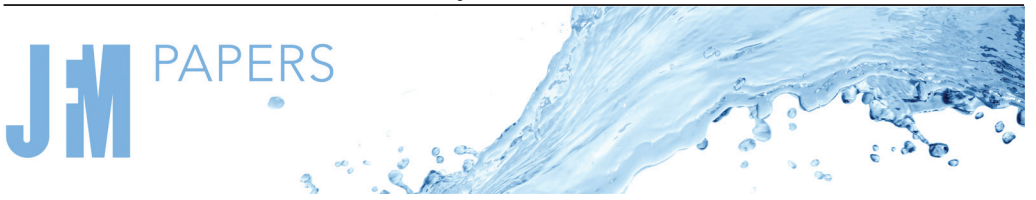

Energetics of buoyancy-generated turbulent flows with active scalar: pure buoyant plume

Chang Hsin Chen[1],‡ **and Kiran Bhaganagar**[1],†

[1]Laboratory of Turbulence, Sensing and Intelligence Systems, Department of Mechanical Engineering, The University of Texas at San Antonio, One UTSA Circle, San Antonio, TX 78249, USA

(Received 16 April 2022; revised 25 October 2022; accepted 29 November 2022)

A framework for the budget of Reynolds stress, temperature and density variations, turbulent mass flux and turbulent heat flux is presented for buoyancy-generated turbulent flows with a focus on turbulent plumes. The dynamical interactions between the turbulence generated from the velocity and thermodynamic fluctuations in thermal and heated gas plumes is studied. A large-eddy simulation tool has been used to simulate heavier and lighter than air plumes released from a circular heated source for high Reynolds number (*Re*). The budget equations are developed using a Favre-averaging approach. Both heated air plumes and heated gas plumes, namely, heated SO_2 and heated CH_4 plumes, are included in the study. The study focuses on addressing key questions – does the turbulence kinetic energy (TKE) spectrum follow the classical inertial $-5/3$ spectrum or is there a -3 buoyancy regime with a different scaling law? Fundamental pathways for generation of turbulence through velocity fluctuations, and temperature and density fluctuations are discussed. Analysis of the TKE and scalar variance budget equations has demonstrated that multiple mechanisms dominate the transport of Reynolds stresses, and in particular that correlations between the density and the velocity dominates the turbulence production mechanisms. Entrainment is connected to the turbulent transport and pressure-dilation processes.

Key words: plumes/thermals, turbulence simulation, turbulent convection

1. Introduction

For incompressible, turbulent flows at a low Mach number, when the buoyancy effects are dominant, the variations in density are substantial and, in fact, dominate the flow

† Email address for correspondence: kiran.bhaganagar@utsa.edu
‡ Present address: Department of Mechanical Engineering, University of Connecticut, Storrs, CT 06269, USA.

physics. In these flows, the scalar field (temperature, density or concentration) cannot be considered a passive variable. In turbulent flows in which temperature/density is a passive scalar, thermal/concentration fluctuations are produced by instabilities in the velocity field (Lumley & Panofsky 1965; Wyngaard & Coté 1971). In contrast, buoyancy forcing introduces variable density effects that modify turbulence transport and production mechanisms. In pure buoyancy-driven flows, the scalar gradients are coupled to the momentum through the buoyancy term (density–gravity term) as a source term in the momentum equation. This is very different from the case of momentum-driven flows, such as turbulent jets, in which scalar fields, such as temperature and concentration of species, are passive and hence uncoupled from the momentum. In particular, a density field is required to determine buoyancy effects in a buoyant flow. Therefore, it is necessary to simultaneously measure both density and velocity fields. The combined temporally and spatially resolved velocity and density data are then used to determine parameters such as the Favre-averaged velocity and turbulence statistics. Hence, experimental data are limited (Shabbir & George 1994; O'Hern *et al.* 2005). Large-eddy simulation (LES) has been used to study buoyancy-driven convection and successfully resolve the turbulence (Nieuwstadt & de Valk 1987; Bastiaans *et al.* 2000; Pham *et al.* 2007; Yan 2007; Devenish *et al.* 2010; Bhimireddy & Bhaganagar 2021; Chen & Bhaganagar 2021).

Turbulent buoyant plumes are generated by a continuous supply of buoyancy, such as a thermal source or a release of gas, and are very significant in both natural and engineered systems. Due to the spatial variations of the density, a turbulent plume is formed that actively mixes with the ambient. This mixing of the ambient fluid with the plume is entrainment. The lighter (or denser) fluid entrains the surrounding ambient heavier (or lighter) fluid through the plume interface. This is a fundamental fluid dynamic problem which is very complicated and still not well understood. A systematic comparison of different entrainment theories was summarized a few years ago (van Reeuwijk & Craske 2015). Nonlinear mechanisms result in the simultaneous generation of velocity fluctuations and temperature (and density) fluctuations. Further, a combination of shear- and buoyancy-generated processes contribute to the production of turbulence (Wyngaard & Coté 1971; Darisse, Lemay & Benaïssa 2015; Charonko & Prestridge 2017). The focus of this manuscript is to make significant advancement in understanding the dynamical interactions between the thermodynamics and the flow in the generation of turbulence and the transport processes in buoyant plumes. Most of the works on free-shear flows have focused on turbulent jets, however, our current understanding of the turbulence energetics for pure buoyancy-generated convection is extremely limited. Buoyancy-generated turbulence processes with substantial density variations within the flow are critical in applications such as thermal convection in the atmosphere; wildland smoke plumes; mixing of different density fluids in an acceleration/gravitational field, as in Rayleigh–Taylor (Rayleigh 1882; Taylor 1950) and Richtmyer–Meshkov (Richtmyer 1960; Meshkov 1969) instability flows; and mixing of the temperature and salinity fields in large-scale ocean currents and the thermohaline circulation (Adkins, McIntyre & Schrag 2002; Wunsch 2002; Wunsch & Ferrari 2004). Theory, modelling and even empirical knowledge of turbulence processes in buoyancy-generated turbulence are less well developed (Chen & Rodi 1980; Gouldin *et al.* 1986; Pitts 1986; Dimotakis 2005).

Experiments and numerical simulations of buoyant plumes have contributed to our understanding of the scaling laws of the mean flow and turbulence intensity. Plumes attain self-similar radial profiles for both the mean axial velocity and the mean temperature (Shabbir & George 1994; Ezzamel, Salizzoni & Hunt 2015; Bhimireddy & Bhaganagar 2021). Batchelor (1954) and Morton, Taylor & Turner (1956) have proposed similarity

solutions for mean axial velocity and mean buoyancy in terms of B_o, the rate at which buoyancy is added at the source, z, height, r, radial distance, and g', buoyancy acceleration. Recently, the LES of area-released thermal plumes at high Reynolds numbers and for very high surface heat flux conditions conducted by Bhimireddy & Bhaganagar (2021) demonstrated that the radial profiles of mean temperature and mean buoyancy reach a self-similarity state with a Gaussian distribution. In their study, the LES was in good agreement with the theoretical prediction of the $-1/3$ and $-5/3$ power laws for the centreline mean temperature difference and mean velocity of an axisymmetric plume. The axial mean velocity develops a similarity solution of the form $\overline{w_c} = B_o^{1/3} z^{-1/3} e^{A_1 (r/z)^2}$ and the axial buoyancy has a form $\overline{\theta_c} = B_o^{2/3} z^{-5/3} e^{A_2 (r/z)^2}$, where $\overline{w_c}$ and $\overline{\theta_c}$ denote the mean centreline velocity and temperature, respectively, and A_1 and A_2 correspond to the Gaussian similarity coefficients for $\overline{w_c}$ and $\overline{\theta_c}$. Higher-order turbulent quantities such as turbulent intensity and turbulent stresses also evolve with self-similar radial profiles (Papanicolaou & List 1988; Wang & Law 2002; Ezzamel *et al.* 2015). The experiments of Shabbir & George (1994) and LES of Bhimireddy & Bhaganagar (2021) have shown that, for thermal plumes, turbulence reaches a quasi-steady values as follows: the range for root-mean-square values of axial velocity fluctuations (w_{rms}) is 0.31–0.35, radial velocity fluctuations (u_{rms}) is 0.21–0.24 and temperature fluctuations (θ_{rms}) is 0.48–0.53.

The budget equations for the Reynolds stresses and the temperature and scalar variance will provide insights into modelling of the velocity and scalar fields and understanding of the interactions between these fields. In particular, it is important to understand what the differences are in the energetics between a passive scalar and an active scalar. Most of the analyses of the energetics on buoyancy-driven flows (turbulent jets and plumes) have focused on buoyant jets in the regime in which the momentum flux dominates the buoyancy flux (Pitts 1991*a*,*b*; Panchapakesan & Lumley 1993; Chassaing, Harran & Joly 1994; Amielh *et al.* 1996; Djeridane *et al.* 1996; Talbot, Aftabi & Chemia 2009; Charonko & Prestridge 2017). The results have revealed that, similar to variable-density shear layers, Rayleigh–Taylor and Richtmyer–Meshkov mixing, the effect of variable density mixing in buoyant jets is mainly observed in the modification of the turbulent mass flux and gradient stretching processes to turbulent kinetic energy (TKE) production (Charonko & Prestridge 2017).

Additional insight into the energetics can be obtained from the TKE and the scalar spectrum. For turbulent mixing of a passive scalar, the works of Kolmogorov (1941), Obukhov (1949) and Corrsin (1951) have established a one-dimensional scalar spectrum that follows the $-5/3$ law of the power spectra. However, it is not clear if this scaling holds good for an active scalar as well. Some experimental evidence indicates that the spectral energy decays faster than the $-5/3$ power of the wavenumber and contradicts the theoretical predictions at higher wavenumbers in the plume region (Papanicolaou & List 1988). Chen & Bhaganagar (2021) observed the existence of a -3 power law for the energy spectra at low wavenumbers. This study was the first one to reveal the existence of a buoyancy regime in thermal plumes before the flow transitions to the classical $-5/3$ inertial regime.

Turbulent mixing contributes significantly to entrainment, as both shear- and buoyancy-generated sources contribute to the generation of TKE. With an active scalar transport, we hypothesize that a combination of velocity and thermodynamic instabilities dominate the turbulence production processes. Reynolds stresses and the correlations of temperature and velocity fluctuations, as well as density and velocity fluctuations, play an important role in turbulence generation. In this work, we address the following questions:

What are the fundamental pathways for generating turbulence (source terms of the TKE equation vs those of temperature variance equations vs those of the density variance equation)? What are the dominant transport processes (pressure distribution vs turbulence transport, turbulent mass transport and turbulent heat transport)? What is the nature of the spectra of velocity, temperature and density fluctuations? An in-house LES tool will be used to resolve the turbulence.

The overall goal of the study is to improve our understanding of the energetics and the turbulence budget mechanisms for pure buoyancy-generated flows. In the present work, we analyse the transport processes of Reynolds stresses, the temperature variance and density variance in the axial and horizontal directions, along with the spectral analysis of TKE, temperature and density fluctuations to understand the key mechanisms that contribute to turbulence production, transport and mixing processes. The budget equations of turbulent mass and heat flux will provide an understanding of the transport processes. It should be noted that the Favre-averaged Reynolds stresses have a coupling between the density and the velocity fluctuations, and are a measure of the deviation caused due to the variable-density nature of the flows. To the authors' knowledge, this is the first time wherein the energetics are derived and analysed for pure buoyant plumes.

The rest of the paper is organized as follows. In § 2, the numerical method and problem set-up are discussed. Section 3.1 focuses on the TKE budget analysis. In § 4, the fluctuations of thermodynamic variables are discussed, including the transport equations and spectra. The correlations of TKE and thermodynamic variables and the dominant mechanisms are addressed in § 5. Finally, the conclusions are presented in § 6.

2. Large-eddy simulation

2.1. *Governing equations*

Large-eddy simulation within a weather research and forecasting (WRF) model was developed and validated to simulate thermal buoyant plumes (Bhaganagar & Bhimireddy 2020*b*; Bhimireddy & Bhaganagar 2021). A thorough performance assessment of WRF has been conducted to accurately resolve the micro-scale turbulence (Bhaganagar & Bhimireddy 2017; Bhimireddy & Bhaganagar 2018*a*,*b*; Bhaganagar & Bhimireddy 2020*a*). For the sake of completeness, the numerical framework is presented here. The governing equations are the compressible Euler equations with eddy viscosity and gravitational forces as follows:

$$\frac{\partial \rho}{\partial t} + \frac{\partial \rho u_i}{\partial x_i} = 0, \tag{2.1a}$$

$$\frac{\partial \rho u_i}{\partial t} + \frac{\partial \rho u_j u_i}{\partial x_j} = -\frac{\partial p}{\partial x_i} + \frac{\partial \tau_{ij}}{\partial x_j} - \delta_{3i}\rho g, \tag{2.1b}$$

$$\frac{\partial \rho \theta}{\partial t} + \frac{\partial \rho u_j \theta}{\partial x_j} = \frac{\partial}{\partial x_j}\rho Pr_t^{-1}\mu_t \frac{\partial \theta}{\partial x_j} - \delta_{i3}\frac{h_0 g}{C_p}, \tag{2.1c}$$

$$\frac{\partial \rho q_m}{\partial t} + \frac{\partial \rho u_j q_m}{\partial x_j} = \frac{\partial}{\partial x_j}\rho Pr_t^{-1}\mu_t \frac{\partial q_m}{\partial x_j} + Q_p, \tag{2.1d}$$

$$\frac{\partial \rho K}{\partial t} + \frac{\partial \rho u_j K}{\partial x_j} = \mu_t \left(\frac{\partial u_i}{\partial x_j} + \frac{\partial u_j}{\partial x_i}\right)^2 - \mu_t N^2 - \rho \frac{CK^{3/2}}{l}, \tag{2.1e}$$

where ρ is the mixture density, u_i is the velocity component in the i direction, θ is the potential temperature, q_m is the mass fraction of the mth species and K is the

modelled TKE. Also, p is the pressure, τ_{ij} is the modelled stress tensor given by $\tau_{ij} = \mu_t(\partial_j u_i + \partial_i u_j - (2/3)\delta_{ij}\partial_k u_k$, δ is the Kronecker delta function, C_p is the specific heat capacity at constant pressure and h_0 is the heat flux applied at the source only. The gravitational term g is considered as a body force, which acts in the negative vertical direction. The eddy viscosity, μ_t, is defined as $\mu_t \equiv C_k l\sqrt{K}$ where $C_k = 0.1$ and l is a length scale given as $l = \min[(\Delta x\Delta y\Delta z)^{1/3}, 0.76\sqrt{K}/N]$ if $N > 0$, otherwise $l = (\Delta x\Delta y\Delta z)^{1/3}$. The Brunt–Väisälä frequency, N, is computed as $N^2 = (g/\theta)\partial_3\theta$.

Further, Pr_t is the turbulent Prandtl number which is defined as $Pr_t^{-1} = 1 + 2l(\Delta x\Delta y\Delta z)^{-1/3}$. From observations, $Pr_t \gtrsim 0.66$ along the centreline in all plumes.

Ideal gas is assumed in the equation of state, and therefore, potential temperature can be related in the equation of state, $p = p_0(\rho R\theta/p_0)^\gamma$, where R is the specific gas constant and γ is the specific heat ratio. In the following discussion, horizontal and vertical velocities, u_1 and u_3, will be presented as u and w. For the spatial directions x_1 and x_3, they will be replaced by x and z.

Besides the small-scale turbulence modelled in (2.1*e*), large-scale quantities, including density, velocities, temperature and mass fraction, are resolved in the conservation laws (2.1*a–d*). Note that density (ρ) is calculated based on the local mass fraction. In addition, the system simulates buoyancy effects without the Boussinesq assumption.

2.2. *Physical problem*

The physical problem that is being investigated in this study is as follows: the physical domain is filled with ambient fluid that is at rest and maintained at a constant temperature. A circular region of the source at the bottom boundary with diameter D(=400 m) is heated with a constant surface heat flux (h_0). The heating causes a temperature difference between the surface and the ambient fluid and convection is initiated (see figure 1). In this work, three different gases are studied: heated air (thermal), heated methane (CH_4) and heated sulphur dioxide (SO_2). In addition to the surface heat flux, for CH_4 and SO_2 cases, the gases are released with a constant surface density flux at the source. Chemical reactions and phase change are not considered in the presented simulations.

A representation of turbulent buoyant plume is shown in figure 1, in which the λ_2-criterion is plotted. A buoyancy source at the bottom of the domain generates an upward buoyancy flux which induces entrainment of the ambient fluid as the plume rises. Turbulence velocity fluctuations and temperature fluctuations are generated by the plume.

The coordinate system is Cartesian, and the horizontal directions are represented by the x and y axes and the vertical direction is represented by the z axis. The domain size, $(L_x, L_y, L_z) = (10D, 10D, 17.5D)$. The initial conditions are the hydrostatic pressure conditions, $\partial_3 p = -\rho g$, and the equation of state with reference state specified at the sea level. Additionally, zero velocity conditions are imposed throughout the domain due to quiescent ambient conditions. Periodic boundary conditions are imposed on the horizontal (transverse) direction. At the top of the domain, a constant pressure is specified based on hydrodynamic relations and a no-slip condition is imposed at the bottom.

The simulations have been performed for seven different cases. The details of the cases are provided in table 1. Cases 1–5 represent the release of heated air referred to as the thermal plume. The surface heat flux h_o for these cases varies in the range 0.0044–0.024 kg s^{-3}. Cases 6 and 7 are for CH_4 and SO_2 released with h_o of 0.024 kg s^{-3}.

The Reynolds and Froude numbers are calculated based on time-averaged flow variables after the plumes reach the stationary state. The dimensional parameters are h_0, g_0', $\Delta\rho$ and R; the resulting non-dimensional parameters are the Reynolds number

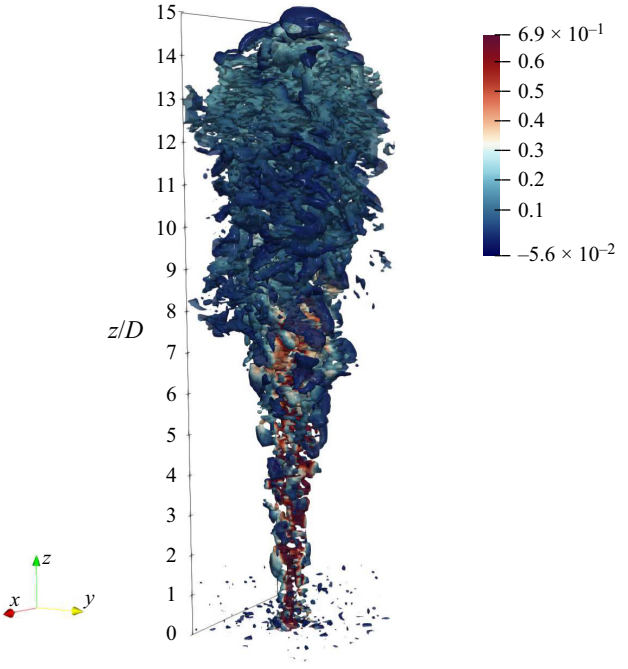

Figure 1. The λ_2 vortex criterion (Jeong & Hussain 1995) of a thermal turbulent buoyant plume coloured with ambient temperature subtracted from potential temperature.

Case	1	2	3	4	5	6	7
species	air	air	air	air	air	CH_4	SO_2
R	287	287	287	287	287	159	638
h_0 (kg s^{-3})	4.4×10^{-4}	8.8×10^{-4}	1.3×10^{-3}	1.8×10^{-3}	2.4×10^{-3}	2.4×10^{-3}	2.4×10^{-3}
$\Delta\rho$	0.988	0.977	0.972	0.967	0.961	0.979	0.971
g_0' (m s^{-2})	0.082	0.145	0.185	0.237	0.272	0.189	0.061
Γ	0.80	0.76	0.74	0.71	0.68	0.65	0.8
l^*	0.31	0.32	0.35	0.37	0.37	0.7	0.5
z^*	1.62	1.63	1.63	1.75	1.75	6.35	2.08
Re	6.02×10^7	9.12×10^7	1.15×10^8	1.33×10^8	1.47×10^8	7.00×10^7	5.38×10^7
Re_t	9.9×10^5	1.7×10^6	2.0×10^6	2.1×10^6	2.2×10^6	1.7×10^6	1.6×10^6
Re_{sgs}	4.4×10^3	4.4×10^3	4.4×10^3	4.4×10^3	4.4×10^3	2.1×10^3	4.5×10^3
R_K	0.20	0.14	0.13	0.15	0.15	0.05	0.1
M	1.8×10^{-2}	2.4×10^{-2}	2.6×10^{-2}	3.1×10^{-2}	3.4×10^{-2}	3.0×10^{-2}	1.4×10^{-2}
M_t	3.8×10^{-3}	5.9×10^{-3}	6.2×10^{-3}	7.8×10^{-3}	8.0×10^{-3}	8.8×10^{-3}	6.5×10^{-3}
Fr	1.091	1.089	1.110	1.141	1.149	1.149	1.1629
At	2.35×10^{-2}	2.30×10^{-2}	2.35×10^{-2}	2.61×10^{-2}	2.69×10^{-2}	8.77×10^{-2}	2.95×10^{-2}

Table 1. Scaled parameters of the source and the plume: R is the specific gas constant, h_0 is the heat flux of the source; $\Delta\rho = (\rho_0 - \rho_\infty)/\rho_\infty$ is the density difference between the source (ρ_0) and the ambient (ρ_∞); g_0' is the initial reduced gravity at the source defined as $g_0' = (T_0 - T_\infty)g/T_0$, where T_0 is the temperature at the source and T_∞ is the ambient temperature; z^* is the streamwise location of maximum mean velocity normalized by D; l^* is the half-width of the plume at z^* normalized by D. The following dimensionless quantities are measured at z^*: $Re = \bar{w}l^*/\nu$ with viscosity obtained from the air temperature while $Re_t = w''l^*/\nu_t$ with eddy viscosity ν_t; $Re_{sgs} = \sqrt{TKE_{sgs}}\Delta z/\nu_t$, where sgs represents subgrid scale; R_K is the ratio of subgrid-scale TKE to the resolved TKE; $M = \bar{w}/c$, where c is the speed of sound; $M_t = w''/c$; $Fr = w/\sqrt{g_0'D}$ and $At = (\rho_0 - \rho)/(\rho_0 + \rho)$.

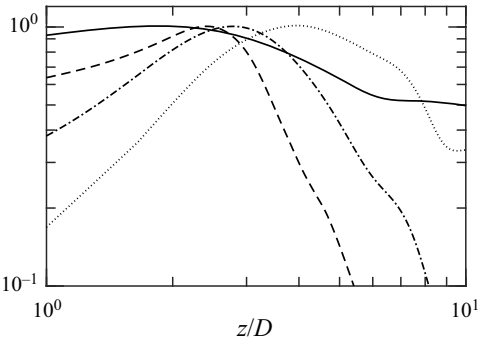

Figure 2. The axial distributions of mean axial velocity ($\bar{w}$, solid), density variance ($\overline{\rho'^2}$, dashed), vertical turbulent heat flux ($\widetilde{T'w''}$, dash-dotted) and axial Reynolds stress (R_{33}, dotted) along the centreline for case 5.

and the Froude number. The resolution for all the simulations is $100^2 \times 700$. The grid-independence test increased the resolution from $40^2 \times 250$ to $200^2 \times 1400$, and found that the temporal-spatial evolution of both centreline velocity and the plume height saturate at $100^2 \times 700$. The simulations have been validated by comparing the mean centreline velocity and plume height against experimental measurements (Ai, Law & Yu 2006) and with theoretical analysis (Bhamidipati & Woods 2017). Good agreements were obtained with those predictions in the literature. In addition, comparison between $100^2 \times 700$ and $200^2 \times 1400$ showed that the relative errors of the resolved vorticity are $<2\,\%$ and the error of the modelled dissipation is $O(10^{-6})$.

When buoyant plumes rise from their sources, their structures begin developing as the heat is transferred to the mean flows. Such energy transfer further results in the generation of TKE, thermodynamic fluctuations and other turbulent structures. Figure 2 shows the spatial distributions of mean flow and other turbulent variables along the centreline from case 5. Starting at the source, all the quantities have a monotonic increase and reach their maximum. Mean vertical velocity, $\tilde{w}$, peaks first at $z/D \approx 2$, followed by $\overline{\rho'^2}$ and $\widetilde{T''w''}$ at $z/D \approx 3$. Finally, the vertical fluctuating velocity, w'', reaches its peak last at $z/D \approx 5$. The following discussion shows a strong dependence of the plume structures on these three characteristic locations. The values of $\widetilde{T''^2}$ and $\overline{\rho' w''}$ show similar distributions to $\overline{\rho'^2}$ and $\widetilde{T''w''}$, and therefore are not presented.

3. Statistics of Reynolds stresses

3.1. *Spatial distributions*

The notation used in this manuscript is as follows – for an instantaneous flow variable q, the Reynolds time-averaged quantify ($\bar{q}$) is defined as $\bar{q} = \Sigma_i^n q_i/n$, where, n is the number of instantaneous time steps after the flow reached stationary state. Unless otherwise stated, the normalization has been performed based on the maximum value along the centreline. The symbol * denotes the normalized value with respect to the maximum value at the centreline. The Favre-averaged variable is defined as $\tilde{q} = \overline{\rho q}/\bar{\rho}$. The Favre-averaged fluctuations are, therefore, defined as $q'' = q - \tilde{q}$. For the rest of the manuscript, fluctuations represent the Favre-averaged fluctuations. Tensor notation

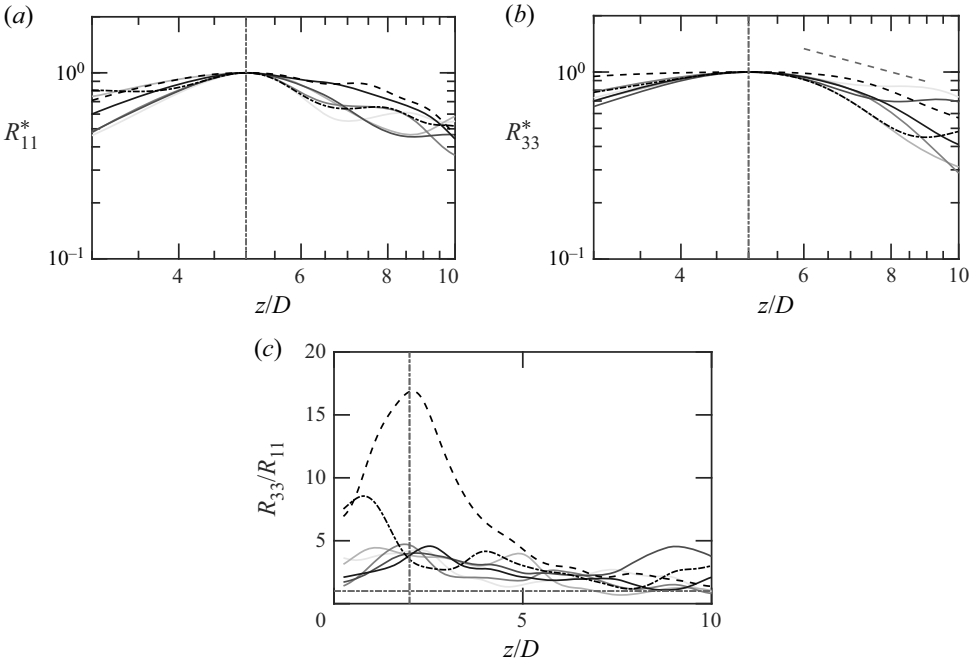

Figure 3. (*a*) Centreline distributions of R_{11} normalized by the peak value. (*b*) Centreline distributions of R_{33} normalized by the peak value. (*c*) Ratio of R_{33} and R_{11} at the centreline. Solid lines: thermal plumes (grey), methane (black, dashed) and sulphur dioxide (black, dash-dotted). Solid lines: thermal plumes, grey levels from light to dark correspond to case 1–5 in ascending order. Black dashed and dash-dotted lines represent methane and sulphur dioxide plumes, respectively. Grey dash-dotted lines: $z/D = 2$ (vertical) and $R_{33}/R_{11} = 1$ (horizontal).

is used to represent all higher-order tensors. The Reynolds stresses, $R_{\alpha\alpha}$ are defined as $R_{\alpha\alpha} \equiv \widetilde{u''_\alpha u''_\alpha}$.

We begin the analysis by examining the axial distribution of axial (R^*_{33}) and horizontal (R^*_{11}) components of the TKE, as plotted in figure 3(*a*,*b*). Here, R_{11} is the average from both transverse directions. since our data show that the plumes are axisymmetric. The existence of two plume distinct regimes – the initial and the mixing stages are evident. It should be noted that for starting plumes, the mean flow accelerates from rest and reaches a maximum velocity at around $2D - 3D$ above the source. Meanwhile, TKE reaches its maximum near $z/D = 5$. This stage ($z/D \lesssim 5$) is referred to as the initial stage. During the initial stage, turbulence (velocity fluctuations and thermodynamic fluctuations) is still developing and without significant radial expansion (see figure 1).

The plume next enters the mixing stage in which the turbulence starts to decay; meanwhile, much more significant radial expansion is observed. This stage is referred to as the mixing stage. This occurs around $z/D > 5$. During the initial stages, both the components of the Reynolds stresses increase from the source value and reach their peak value at $z/D \approx 5$, beyond which they decrease exponentially with an exponent of -1 during the mixing stage. Even though a minor scatter exists in the mixing stage, the comprehensive analysis shows a consistent and monotonic decrease in the region from $z/D = 5$ to $z/D = 17.5$. Similar spatial trends have been observed for other thermal, CH_4 and SO_2 cases. There is no observable trend with Reynolds number. To further understand the differences between the components of the Reynolds stresses, the ratio of R_{33} and

R_{11} is plotted in figure 3(*c*). Unlike R_{33} and R_{11} which peak at around $5D$, R_{33}/R_{11} peaks at approximately $2D$ instead. Further ahead, this ratio decreases with height and it slowly approaches an asymptotic value of unity. This suggests a tendency towards isotropy. The approach-to-isotropy process indicates that, further away from the source, the two components of the Reynolds stresses are dominated by similar mechanisms.

For thermal plumes, monotonic increase with Re and Fr is observed in the maximum value of R_{33}/R_{11}. Such trends are reasonable as budget analysis will later reveal that buoyancy is a dominant mechanism in the Reynolds stress and dissipation is a counterpart. For species plumes, the difference can be realized through the Atwood number as high At is associated with increasing mixing in buoyancy-driven flows (Luo *et al.* 2020; Taha *et al.* 2022).

3.2. *Budget analysis*

To understand the mechanisms that control the Reynolds stresses, the budget equation for Reynolds stresses is presented next

$$\bar{\rho}\tilde{u}_k\frac{\partial R_{\alpha\alpha}}{\partial x_k} = P_B + P_S + \Pi + \epsilon + M + \mathcal{T}. \tag{3.1}$$

In (3.1), the left-hand term is the mean convection equation On the right-hand side, P_B and P_S are the production terms and Π is the pressure dilatation, ϵ is the dissipation, M is the mass-flux contribution and $\mathcal{T}$ is the summation of all transport terms. The explicit form of each term is given as follows:

$$P_B = -2\overline{\rho' u''_\alpha} g_\alpha \tag{3.2a}$$

$$P_S = -2\bar{\rho}R_{\alpha k}\frac{\partial \tilde{u}_\alpha}{\partial x_k} \tag{3.2b}$$

$$\Pi = 2\overline{p'\frac{\partial u''_\alpha}{\partial x_\alpha}} \tag{3.2c}$$

$$\epsilon = -\overline{2\sigma'_{\alpha k}\frac{\partial u''_\alpha}{\partial x_k}} \tag{3.2d}$$

$$M = 2\overline{u''_\alpha}\frac{\partial \overline{\sigma_{\alpha k}}}{\partial x_k} \tag{3.2e}$$

$$\mathcal{T} = -\frac{\partial \overline{\bar{\rho}u''_\alpha u''_\alpha u''_k}}{\partial x_k} - 2\frac{\partial \overline{p'u''_\alpha}}{\partial x_\alpha} + 2\frac{\partial \overline{\sigma'_{\alpha k}u''_\alpha}}{\partial x_k}. \tag{3.2f}$$

The three terms in $\mathcal{T}$ are turbulent, pressure and viscous transport. The derivation of (3.1) is provided in Appendix A.

To get a better understanding of the contribution of the axial vs the radial components to the TKE, we study the axial and the horizontal components of the TKE budget separately. In addition, TKE is further decomposed into the vertical (R_{33}) and horizontal (R_{11}) components.

The budget terms of R_{33} along the centreline are plotted in figure 4(*a*). The results are shown for case 5 (thermal plume). Each term is obtained using the resolved quantities, except the dissipation, which adopts both the resolved and modelled terms. Among all the terms, buoyancy production is the most dominant mechanism, and pressure dilatation,

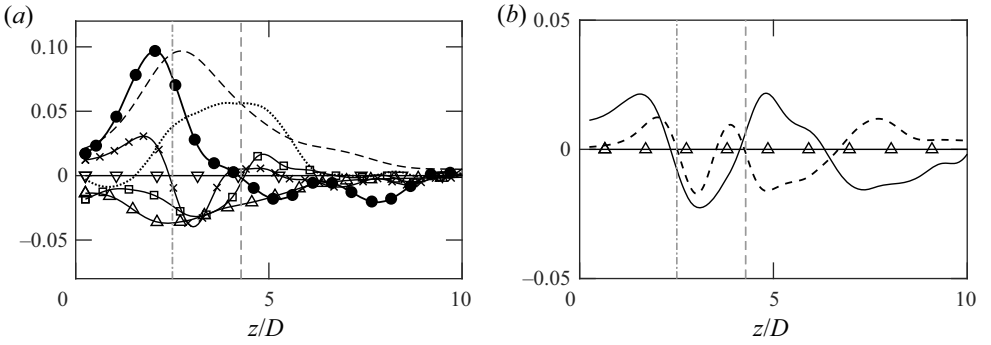

Figure 4. (*a*) Budget of R_{33} from case 5 (thermal plume): convection (•); P_B (−−); P_S (· · ·); Π (□); ϵ (Δ); M (∇); $\mathcal{T}$ (×). (*b*) Decomposition of transport: turbulent transport (dashed); pressure transport (solid); viscous transport (Δ). Vertical grey lines: $\overline{\rho'\rho'}_{max}$ (dash-dotted) and $R_{33,max}$ (dashed).

production by mean flows, transport terms and dissipation are also important. Only the mass-flux contribution is negligible. Due to axial symmetry, production only contains $R_{33}\partial_3\tilde{u}_3$ along the centreline. The spatial evolution along the centreline can be divided into three major regions: buoyant production, pressure-dilatation and dissipation terms increase from the source to $z/D \approx 3$ (as marked by vertical dash-dotted line where $\overline{\rho'^2}_{max}$ occurs), and they peak around $z/D = 3$. Meanwhile, the transport changes sign from positive (towards the source) to negative (away from the source). As the plume continues to ascend from $z/D \approx 3$ to $z/D \approx 5$ (as marked by the vertical dashed line where $R_{33,max}$ occurs), the contributions from buoyancy and dilatation reduce. It is interesting to note, however, that, at the same time, production by mean flows reaches its maximum in this region. During the mixing stage ($z/D \gtrsim 5D$), all the terms decrease and they tend to zero. Comparison of the pressure dilatation and the transport shows that the two terms are counteracting each other far away from the source. Negative pressure dilatation in the initial stage suggests that energy is being transferred out of R_{33} through pressure and dilatation due to strong anisotropy. As the turbulent flows approach an isotropic state in the mixing stage, pressure dilatation is reduced significantly.

Decomposition of the transport terms is shown in figure 4(*b*), and it indicates that viscous transport is negligible while turbulent and pressure transports have similar distributions during the initial stage ($z/D < 5$) near the source. Such trends change completely during the mixing stage, After the plume enters the mixing stage, the two terms start acting against each other. As a result, the overall transport contributions become negligible in the mixing stage. Similar results regarding the budget terms are observed in different gas plumes. Overall, the budget analysis of thermal plumes shows an interesting result that axial velocities are strongly related to density fluctuations as multiple terms change their trends at the peak of $\overline{\rho'^2}$. More discussion regarding such a discovery will be provided in the following sections.

To further understand the most dominant term, the buoyant production terms for the different thermal plumes (cases 1–5) are plotted in figure 5(*a*). With an increasing heat flux at the source, the buoyancy contributions increase correspondingly. For all the cases, the peak production occurs near the corresponding location of $\overline{\rho'^2}_{max}$ regardless of the source conditions. In figure 5(*b*), the buoyancy contributions in thermal, methane and sulphur dioxide plumes with identical heat release are plotted. The peak location shifts

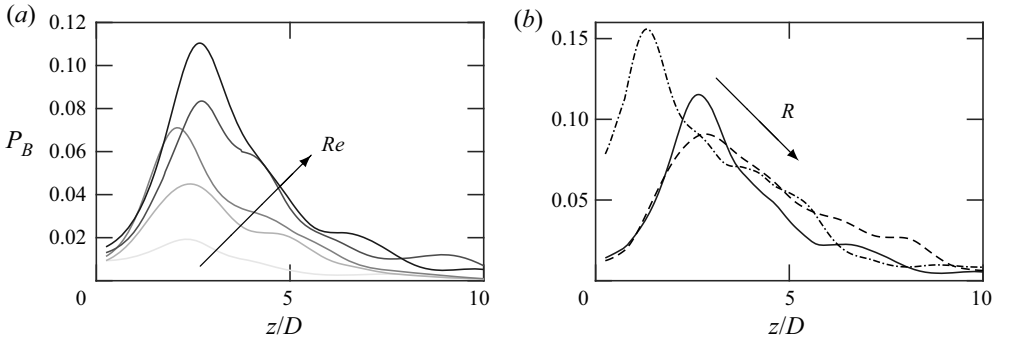

Figure 5. (*a*) Buoyant production of R_{33} in thermal plumes; (*b*) buoyant production of R_{33} in plumes with different species. Same colours as in figure 3.

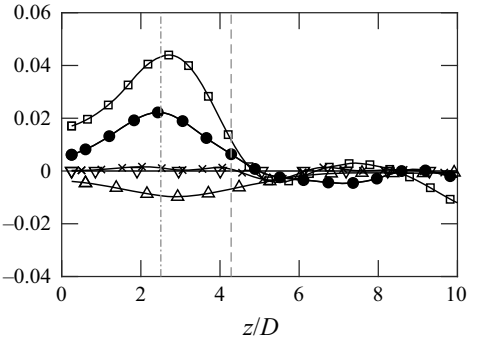

Figure 6. Budget of R_{11} from case 5: convection (•); pressure dilatation (□); mass-flux contribution (∇); transport (×); dissipation (Δ).

toward the source for heavier gases (smaller specific gas constant R). In addition, the heavier is the gas, the higher is the buoyant production. For the same heat release from the source, heavier plumes contain more energy per unit volume, and hence result in stronger buoyancy contributions. For the heavier plumes, the peak location closer to the source is due to the stronger gravitational forces exerted on the gases.

Next, the budget analysis of R_{11} is presented in figure 6. Unlike R_{33}, there is no production term. The figure shows that the transport of R_{11} is strongly dominated by pressure dilatation and dissipation. The dominant pressure dilatation in R_{11} shows that energy is redistributed to R_{11} through pressure and dilatational effects. Similar to R_{33}, R_{11} also shows significant dependence on density fluctuations. Both the dominant terms peak near the maximum of $\overline{\rho'^2}$ near $z/D \approx 3$. A strong dependence on dilatation motions is shown in the transport of R_{11} during the initial stage.

Overall, the TKE budget analysis at the centreline reveals that TKE production is initiated by buoyancy production (closer to the source) in the initial regime of the plume; $R_{ij}\tilde{u}_{i,j}$ becomes important in turbulence generation during the mixing stage. Energy is transferred from the mean flow to axial Reynolds stress. Pressure redistribution is the key process that distributes the energy from the axial to the radial components of Reynolds stress. A complex relation of the pressure transport and turbulent transport drives the mixing of the axial Reynolds stresses. The turbulent transport of the radial Reynolds stress, which will be shown later, plays an important role in the entrainment process.

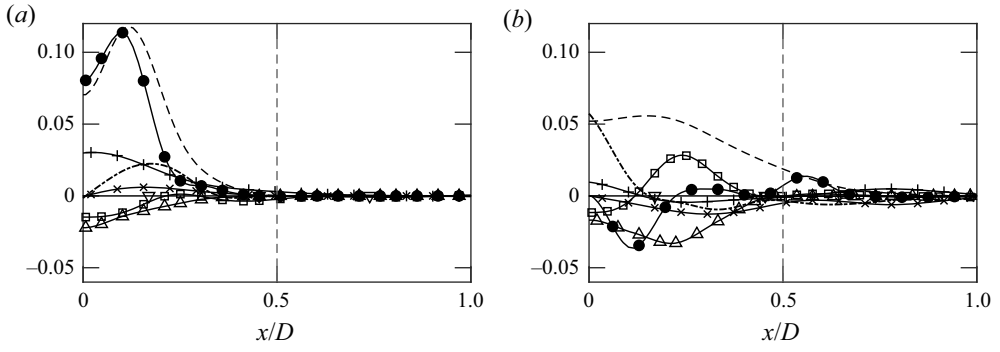

Figure 7. Radial profiles of R_{33} budget from case 5 (thermal plume): convection (•); P_B (−−); P_S (−·); Π (□); dissipation (Δ); M (∇); vertical (+) and horizontal (×) components of $\mathcal{T}$ at (*a*) $z/D \approx 2$ and (*b*) $z/D \approx 5$. Vertical grey dashed lines represent the boundary of the source.

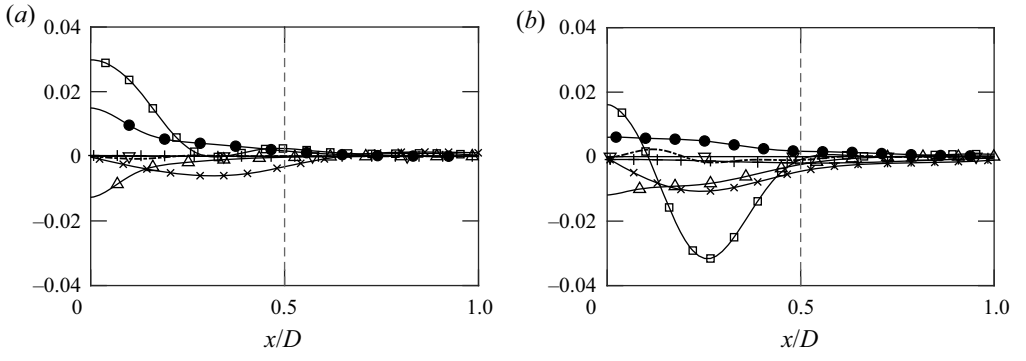

Figure 8. Radial profiles of R_{11} budget from case 5 (thermal plume): convection (•); Π (□); M (∇); ϵ (Δ); vertical (+) and horizontal (×) $\mathcal{T}$ at (*a*) $z/D \approx 2$ and (*b*) $z/D \approx 5$. Vertical grey lines represent the boundary of the source.

Budget analysis along the centreline provides a basic understanding on the turbulent development within the plumes. However, as the plumes enter the mixing stage, significant radial developments are observed. Figure 7 shows the distributions of R_{33} budget terms along the transverse direction at different heights. Both production terms are still the dominant terms along the transverse direction; and peak turbulence production occurs radially away from the centreline. Off-centre peak during the developing stage ($z/D \leqslant 5$) is expected, and slowly disappears during the mixing stage ($z/D > 5$).

The radial profiles of R_{11} terms are shown in figure 8. Near the centreline, pressure dilatation and dissipation are the dominant budget terms. Further away from the centre, transverse transport dominates the budget terms and the direction of the transport is radially towards the centreline. This observation is consistent throughout the plumes at different heights and indicates that the turbulent transport terms are the main contributors to entrainment.

To understand the influence of transport processes on the plume dynamics, the radial profiles of transverse transport terms (with the exception of molecular transport which is insignificant) at a height of $2D$, $5D$ and $10D$ above the source are plotted in figure 9. From the budget analysis of R_{33}, the transport is radially outwards near the source ($2D$).

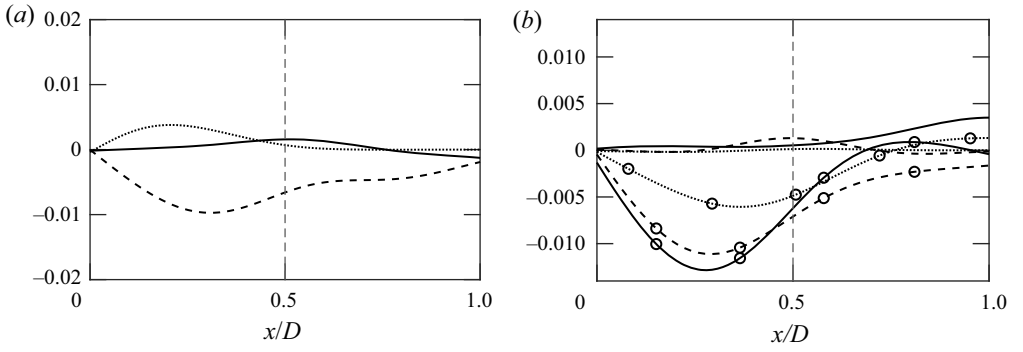

Figure 9. (*a*) Radial profiles of R_{33} turbulent transport terms from case 5 (thermal plume) at $z/D \approx 2$ ($\cdots$), $z/D \approx 5$ ($--$) and $z/D = 10$ ($-$). (*b*) Radial profiles of R_{11} turbulent (lines) and pressure ($\circ$) transport from case 5 at $z/D \approx 2$ ($\cdots$), $z/D \approx 5$ ($--$) and $z/D = 10$ ($-$).

As the plumes transition from the initial to the mixing stage, the direction of transport reverses at $z/D \approx 5$. Near the plume top, i.e. at $z/D = 10$, the transport term becomes negligible. For R_{11}, the radial pressure transport dominates the transport processes at all heights. The radial transport is mainly towards the centreline. Summing the transport processes, turbulence transport is the main mechanism for vertical mixing, while the pressure transport dominates the horizontal mixing processes. The mixing can thus be quantified in terms of turbulent and pressure transport for axial and vertical mixing, respectively.

3.3. *The TKE spectra*

In classical, inertia-dominated turbulence, the source of TKE production is at the large scale and the sink of the turbulence dissipation is at the small scale, and the energy is cascaded in the inertial regime and eventually in the dissipative regime. The spectral slope in the inertial regime follows the classical $-5/3$ power law. In atmospheric turbulence, and in thermally stratified turbulence, the existence of a buoyancy-dominated regime at low wavenumbers has been demonstrated, wherein, the spectral slope of the energy cascading follows the -3 power law. The LES study of Chen & Bhaganagar (2021) demonstrated, for the first time, that the energy spectrum for thermal plumes follows the -3 power law and the energy cascades from the low wavenumber buoyancy regime to the high wavenumber dissipative regimes. To further understand the difference between different species, the energy spectra of thermal, methane and sulphur dioxide plumes are presented at two different heights in figure 10. Here, E_{uu} and E_{ww} represent the energy spectra of horizontal and vertical velocity fluctuations. Similar to the thermal plumes, a buoyancy regime with -3 slope is observed in methane and sulphur dioxide plumes during both the initial and mixing stages. In addition, figure 10 also shows that plumes with lighter gases contain slightly more TKE. Overall, the energy spectra from different species have consistent energy containing buoyancy regimes in their spectra.

Following the proposal of a -3 buoyancy range from Lumley (1964), multiple studies further suggested $E(\kappa) = cN^2k^{-3}$ (Billant & Chomaz 2001; Lindborg 2006). In figure 11, the compensated spectra, $E_{ww}/(N^2k_h^{-3})$ and $E_{uu}/(N^2k_h^{-3})$, at $z/D = 5$ from different plumes are plotted against the wavenumber. The asymptotic states are observed at high

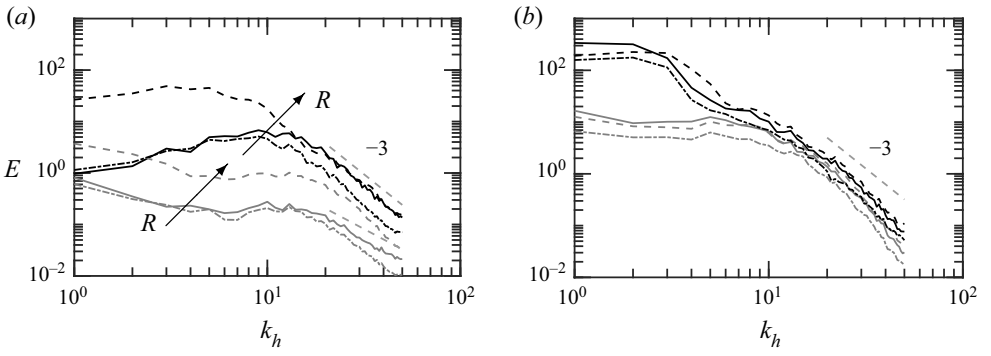

Figure 10. Spectra of vertical (black, E_{ww}) and transverse (grey, E_{uu}) velocities from thermal plume (−), methane (− −) and sulphur dioxide (−·) at (*a*) $z \approx 2D$ and (*b*) $z = 10D$. Here, k_h represents the horizontal wavenumber.

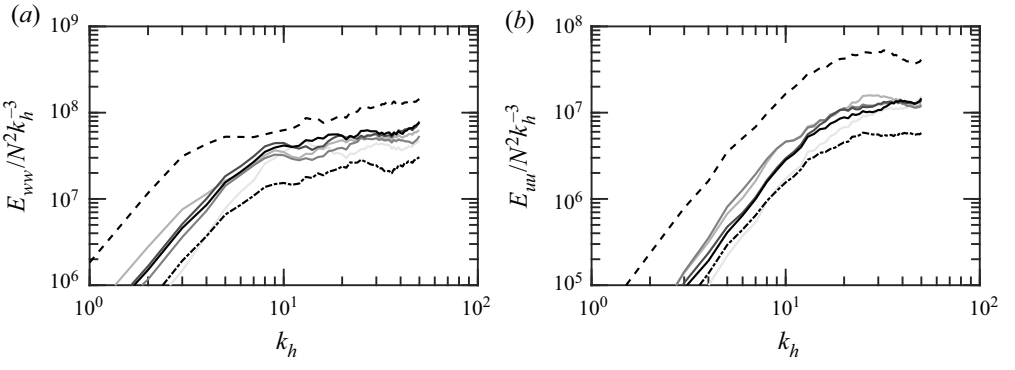

Figure 11. Compensated spectra of (*a*) vertical velocity and (*b*) transverse velocity from thermal (−), methane (CH_4) and sulphur dioxide (SO_2) plumes at $z/D = 5$. Same colours and lines as in figure 3.

wavenumbers for all plumes. Those saturations are also captured when the spectra are presented at different heights for case 5 in figure 12. The plotted compensated spectra clearly show and support the buoyancy range with a −3 spectral slope. From the two figures, we can infer that the coefficient c, instead of being a universal constant, depends on the species and plume height. Further investigations are required to quantify the values of c.

4. Characteristics of thermodynamic fluctuations

In active scalar mixing, the dynamic interactions between the scalar (density and temperature) and the velocity fields generate the temperature fluctuations. This is unlike passive scalar mixing, in which temperature fluctuations are only generated from the velocity fluctuations. The analysis of the temperature variance equation, analogously to the turbulent kinetic energy equation, will provide the answers to the key mechanisms that generate and transport the temperature fluctuations. Further evidence is obtained from the previous discussion, where a connection between the Reynolds stresses and density fluctuations was evident. In the next section, we will discuss the thermodynamic variables that actively contribute to the turbulent plume dynamics.

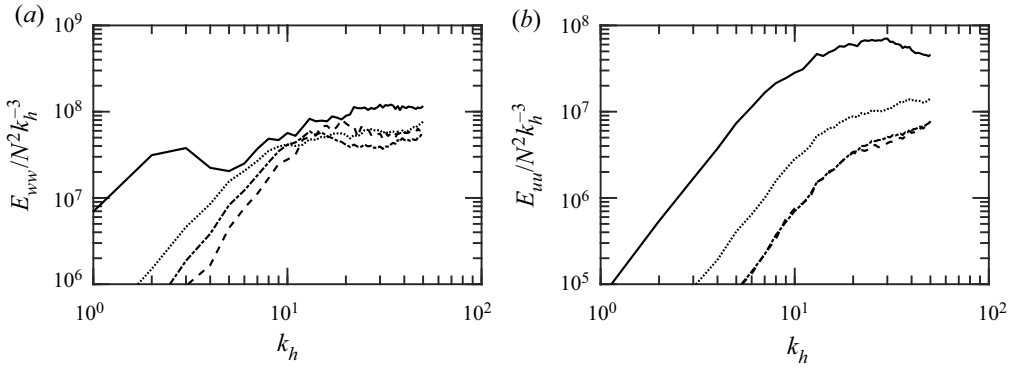

Figure 12. Compensated spectra of (*a*) vertical velocity and (*b*) transverse velocity of thermal plume (case 5) at $z/D = 2$ (−), $z/D = 3$ (−−), $z/D = 5$ (−·) and $z/D = 10$ (···).

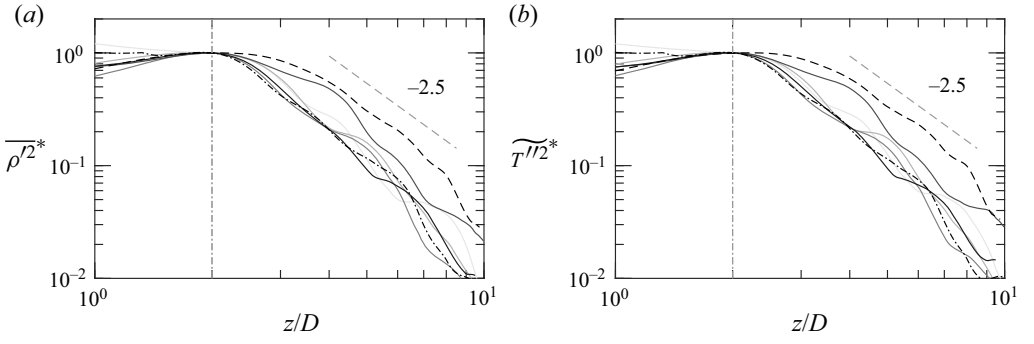

Figure 13. Centreline distributions of (*a*) $\overline{\rho'^2}$ and (*b*) $\widetilde{T''^2}$, each normalized by its maximum. Same lines as in figure 3. All distributions are aligned at $z/D = 2$ (grey, dash-dotted).

4.1. *Statistical scalings*

The streamwise distributions of density and temperature variance, $\overline{\rho'^2}$ and $\widetilde{T''^2}$, along the centreline are shown in figure 13. To have a consistent discussion with the budget analysis, Favre averaging is adopted for temperature.

In addition, the difference between the normalized $\widetilde{T''T''}$ and $\overline{T'T'}$ is $\overline{\rho'T'}^2/\bar{\rho}^2\bar{T}^2 \sim M_t^8$ (Donzis & Jagannathan 2013). Such a difference is negligible under most atmospheric and engineering problems (Donzis & John Panickacheril 2020).

All distributions are normalized by the peak value of the variance. In this figure, the distributions are aligned at $z/D = 2$ since the thermodynamic fluctuations have their peak at around $z/D \lesssim 3$. Similar to the Reynolds stresses, thermodynamic fluctuations increase monotonically from the source to the peak, beyond which they decrease exponentially with an exponent of -2.5. This is much faster compared with an exponent of -1 observed for the Reynolds stresses. As the decay occurs faster compared with Reynolds stresses, this indicates a faster decay of thermodynamic fluctuations with height compared with their velocity fluctuation counterparts. At around $z/D \approx 10$, the fluctuations of density and temperature are already two orders smaller than their peak values.

A different normalization is presented. Figure 14 shows the thermodynamic variances normalized by their local averages. A consistent exponent of -2.3 is observed for all the cases. A clear dependence on Reynolds number and specific gas constant is observed.

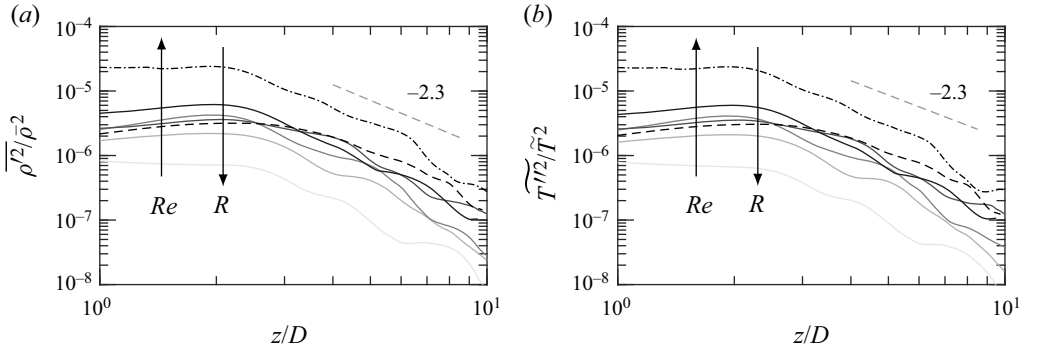

Figure 14. Centreline distributions of (*a*) $\overline{\rho'^2}/\bar{\rho}^2$ and (*b*) $\widetilde{T''^2}/\tilde{T}^2$. Same colours as in figure 3. All distributions are aligned at $z/D = 2$ (grey, dash-dotted).

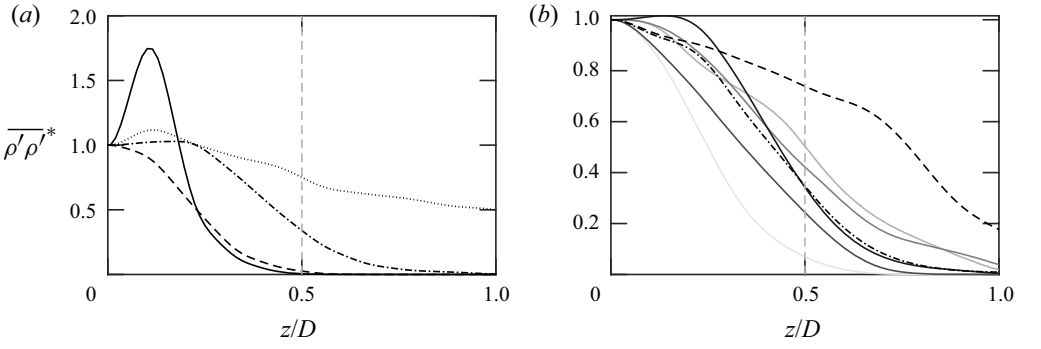

Figure 15. (*a*) Radial profiles of density variances at $z/D = 2D$ (−); $z/D = 3D$ (−−); $z/D = 5D$ (−·); $z/D = 10D$ (···). (*b*) Radial profiles of thermal plumes (−); methane (−−; sulphur dioxide (−·). Solid lines: grey levels from light to dark represent cases 1–5 in ascending order; * represents the normalization by the local centreline values.

With an increasing *Re* or a decreasing *R*, thermodynamic fluctuations increase with respect to their local averages. However, significant differences exist in the normalized values between the plumes. The normalized variances with different source conditions reach an order of 100. Such a dependence implies a stronger acoustic generation with compressibility effects, and those phenomena can have significant impacts on engineering systems and natural environments.

The radial profiles of $\overline{\rho'\rho'}$ at different heights are shown in figure 15(*a*). Near the source ($z/D = 2$), an off-centre peak is observed. The peak decreases significantly with height and disappears before $z/D = 3$. After the density fluctuations reach their peak near $z/D = 3$, an obvious transverse development is observed and the profiles become wider. Figure 15(*b*) further shows the profiles at $z/D = 5$ from different plumes. Despite having different heat releases, the five different thermal plumes have very similar distributions. In addition, the methane plume has slightly wider profiles. Similar to the centreline distributions, $\widetilde{T''T''}$ has very similar distributions to $\overline{\rho'\rho'}$ after normalization.

4.2. *Budget analysis*

To understand physical mechanisms that control the thermodynamic fluctuations, we first look at the transport of the density variance. The budget terms of $\overline{\rho'^2}$ are computed

$$\tilde{u}_j \frac{\partial \overline{\rho'^2}}{\partial x_j} = \mathcal{P}_\rho + P_\rho + \mathcal{T}_\rho + \Pi_\rho + \pi_\rho. \tag{4.1}$$

Similar to (3.1), the term on the left-hand side of the equation is the convection. On the right-hand side of the equation, $\mathcal{P}_\rho$ and P_ρ are the production by the mean flows and density gradient, respectively, $\mathcal{T}_\rho$ is the transport and Π_ρ and π_ρ are the density dilatation connected with the mean flows and fluctuations, respectively. The explicit form of each term is provided as follows:

$$\mathcal{P}_\rho = -2\overline{\rho'^2}\frac{\partial \tilde{u}_j}{\partial x_j} \tag{4.2a}$$

$$P_\rho = -2\overline{\rho' u_j''}\frac{\partial \bar{\rho}}{\partial x_j} \tag{4.2b}$$

$$\mathcal{T}_\rho = -\frac{\partial \overline{\rho'\rho' u_j''}}{\partial x_j} \tag{4.2c}$$

$$\Pi_\rho = -2\bar{\rho}\overline{\rho'\frac{\partial u_j''}{\partial x_j}} \tag{4.2d}$$

$$\pi_\rho = -\overline{\rho'^2\frac{\partial u_j''}{\partial x_j}}. \tag{4.2e}$$

Figure 16(*a*) shows that the evolution of $\overline{\rho'^2}$ is solely dominated by P_ρ and Π_ρ while other terms are at least one order smaller in comparison. From the figure, we can understand that density fluctuations are generated through dilatation terms and diminished due to the turbulence production from density gradient term. Since density and the velocities are negatively correlated, P_ρ is acting as a sink rather than as a source.

While the dilatation term is usually associated with compressibility effect, the effects on the presented plumes are considered small due to the low Mach numbers. Instead, density–velocity correlation, which exists in both P_ρ and Π_ρ, is the main mechanism. The nearly perfect cross-correlation between ρ and w will be discussed in § 5.

Both of the dominant terms peak near $\overline{\rho'^2}_{max}$. The density dilatation (Π_ρ) can be further decomposed into vertical and horizontal components. The two components are plotted in figure 16(*b*). The horizontal and vertical components make opposite but similar contributions throughout the plume. The mirrored distributions of the two different dilatation components indicate that dilatational motions occur when the vertical and horizontal motions are unbalanced. Density fluctuations are generated during this re-distribution process when the flows are anisotropic. During the initial stage, significant contributions of Π_ρ result from strong anisotropy. Such contributions are slowly reduced as the turbulent flows approach isotropy with an ascending plume. Overall, the main contribution for the density dilatation comes from the imbalance of fluctuations through ρ–w cross-correlation. Figure 16(*c*) shows another important term, P_ρ, with different heat sources and gases. With the increasing heat release from the source, P_ρ grows

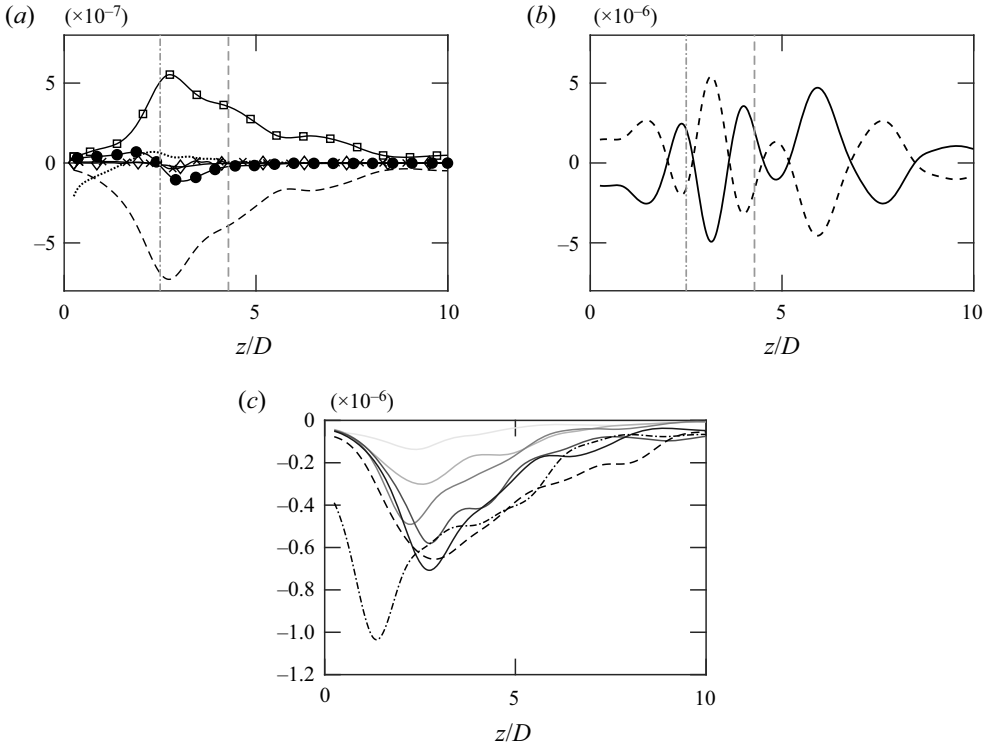

Figure 16. (*a*) Budget of $\overline{\rho'^2}$ from case 5: convection (•); $\mathcal{P}_\rho$ (···); P_ρ (−−); Π_ρ (□); π_ρ (◇); $\mathcal{T}_\rho$ (×). (*b*) Distributions of vertical (−) and horizontal (−−) components of Π_ρ. Vertical grey lines: $\overline{\rho'\rho'}_{max}$ (dash-dotted) and $R_{33,max}$ (dashed). (*c*) Distributions of P_ρ: thermal plumes, grey levels from light to dark correspond to cases 1–5 in ascending order. Black dashed and dash-dotted lines represent methane and sulphur dioxide plumes, respectively.

correspondingly; P_ρ is also found to be more prominent in heavier gases. Although production from mean flow gradients was found to be important to Reynolds stresses, the analogous term, $\mathcal{P}_\rho$, is negligible in the transport of ρ' in buoyant plumes.

The contributions from the pressure and viscous effects are present, hence more terms are involved in the transport of $\widetilde{T''^2}$. The budget analysis of $\widetilde{T''^2}$ is computed

$$\bar{\rho}\tilde{u}_j\frac{\partial\widetilde{T''^2}}{\partial x_j} = \mathcal{P}_T + P_T + \Pi_T + \epsilon_T + \mathcal{T}_T. \tag{4.3}$$

Besides the convection terms on the left side of the equation, $\mathcal{P}_T$ and P_T, on the right side of the equation, are the production from the mean flows and temperature gradient, respectively, Π_T is the temperature dilatation connected with the pressure, $\mathcal{T}_T$ is the sum of all the transport terms and ϵ_T is the dissipation. The explicit form of those budget terms is given as

$$\mathcal{P}_T = -\frac{2}{C_v}\overline{pT''}\frac{\partial\tilde{u}_j}{\partial x_j} + \frac{2}{C_v}\overline{T''\sigma_{ij}}\frac{\partial\tilde{u}_i}{\partial x_j} \tag{4.4a}$$

$$P_T = -2\bar{\rho}\widetilde{T''u_j''}\frac{\partial\tilde{T}}{\partial x_j} \tag{4.4b}$$

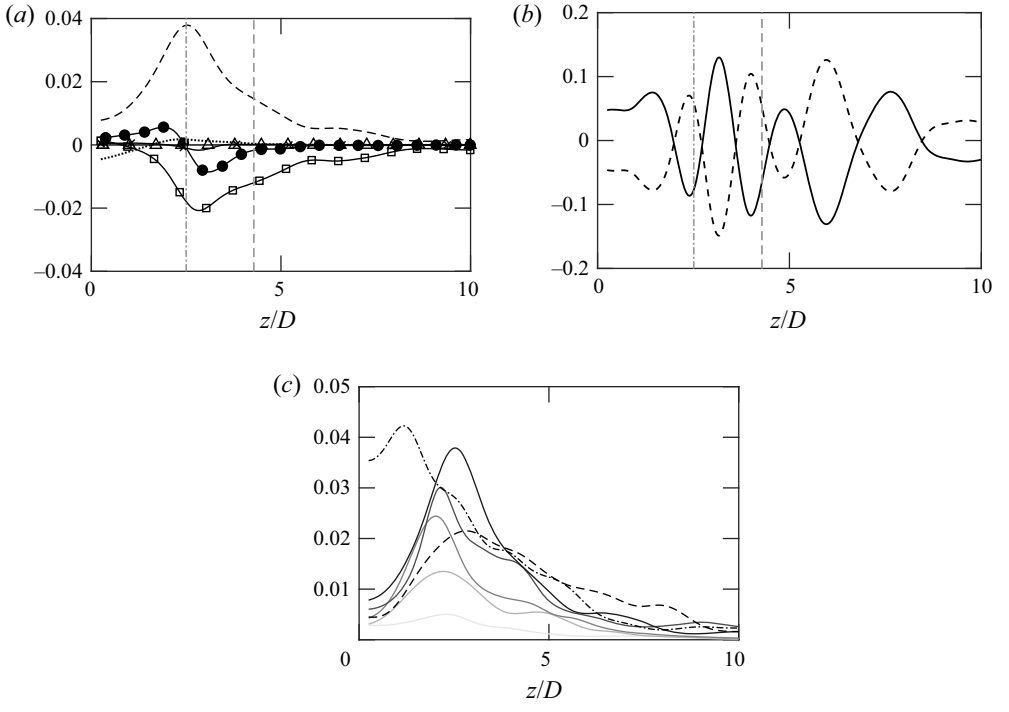

Figure 17. (*a*) Budget of $\widetilde{T''^2}$ from case 5: convection (•); $\mathcal{P}_T$ ($\cdots$); P_T ($--$); Π_T (□); ϵ_T (Δ); $\mathcal{T}_T$ (×). (*b*) Distributions of vertical (−) and horizontal ($--$) components of Π_T. Vertical grey lines: $\widetilde{T''T''}_{max}$ (dash-dotted) and $R_{33,max}$ (dashed). (*c*) Distributions of P_T: thermal plumes, grey levels from light to dark correspond to cases 1–5 in ascending order. Black dashed and dash-dotted lines represent methane and sulphur dioxide plumes, respectively.

$$\Pi_T = -\frac{2}{C_v}\overline{pT''\frac{\partial u_j''}{\partial x_j}} \tag{4.4c}$$

$$\epsilon_T = \frac{2}{C_v}\overline{T''\sigma_{ij}\frac{\partial u_i''}{\partial x_j}} - \frac{2}{C_v}\overline{k_T\frac{\partial T''}{\partial x_j}\frac{\partial T}{\partial x_j}} \tag{4.4d}$$

$$\mathcal{T}_T = -\frac{\partial\overline{\rho T''^2 u_j''}}{\partial x_j} + \frac{2}{C_v}\frac{\partial}{\partial x_j}\overline{k_T T''\frac{\partial T}{\partial x_j}}, \tag{4.4e}$$

where C_v is the specific heat capacity at constant volume, $\mathcal{T}_T$ contains both turbulent and thermal transports and ϵ_T includes viscous and thermal dissipation.

The budget terms in (4.4) are shown in figure 17(*a*). Similar to $\overline{\rho'^2}$, the evolution of $\widetilde{T''^2}$ is dominated by the temperature dilatation and the production of temperature gradient terms.

Section 5 will further show a very strong correlation between T'' and w''. The two dominant budget terms are therefore associated with cross-correlation rather than the compressibility.

In contrast to $\overline{\rho'^2}$, P_T is functioning as a source rather than as a sink, and the dilatational motions are negative. However, the dilatation mechanisms are also significant in the initial

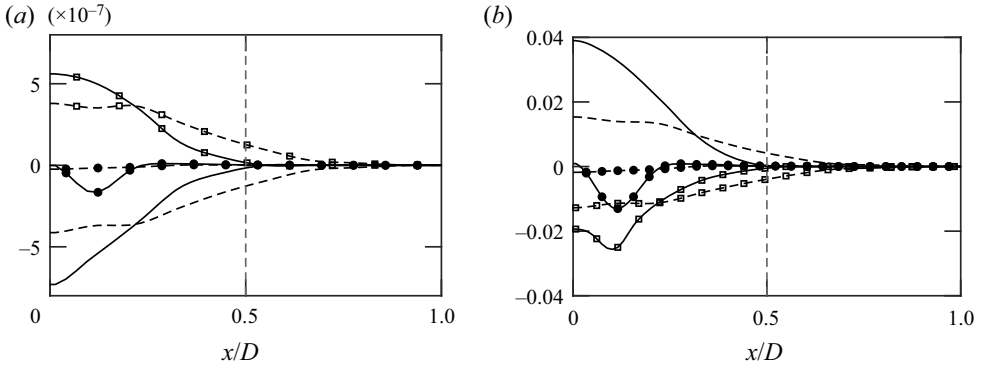

Figure 18. (*a*) Radial profiles of $\overline{\rho'\rho'}$ budgets at $z/D \approx 3$ (solid lines) and $z/D \approx 5$ (dashed lines): $\widetilde{u}_j\partial_j\overline{\rho'\rho'}$ (•); P_ρ (lines); Π_ρ (□). (*b*) Radial profiles of $\widetilde{T''T''}$ budgets at the same heights: $\bar{\rho}\widetilde{u}_j\partial_j\widetilde{T''T''}$ (•); P_T (lines); Π_T (□).

stage in which turbulence is highly anisotropic, just as was observed in $\overline{\rho'^2}$. Further, decomposition of Π_T, as shown in figure 17(*b*), shows opposite distributions of vertical and horizontal dilatations. Similar to density, the dilatational effects occur in response to anisotropic motions and contribute to $\widetilde{T''^2}$. In figure 17(*c*), P_T from different plumes is presented. The production increases with heat source and with increasing density difference between the source and the ambient fluid (i.e. heavier gases).

In addition to the centreline distributions, budget terms are also compared in the transverse directions. Figure 18 shows the dominant terms of $\overline{\rho'\rho'}$ and $\widetilde{T''T''}$. Consistent with the centreline distributions, P_ρ and Π_ρ are still the main mechanisms for density in the radial transport. Similarly, P_T and Π_T are the dominant terms for radial transport of temperature. Other budget terms are negligible, and thus they are not included in the figure.

4.3. *Thermodynamic spectra and baroclinicity*

Besides the knowledge of the spatial development, it is also important to understand at what scales the thermodynamic fluctuations exist. Figure 19(*a*,*b*) shows the evolution of two-dimensional horizontal spectra of density and temperature in wave space. As the plumes ascend, the mixing processes reduce the energy content of the plumes. Although the magnitude of the spectra drops significantly over the intermediate scales, a slight increase is observed at the larger scales. The decrease at intermediate wavenumbers reveals larger Taylor microscales. Such an impact on the plume structure and other physical/chemical phenomena requires further investigation. It is interesting to note that a consistent spectral slope of -2.7 is observed throughout the plume for both density and temperature fluctuations. In the literature of stratified turbulence, a range of slopes has been reported from -2.5 (Waite 2011) to -3 (Carnevale, Briscolini & Orlandi 2001). The spectral slope in the present work is consistent with the reported range.

The density and temperature spectra of thermal, methane and sulphur dioxide plumes at two different heights are plotted in figures 20(*a*,*b*) and 21(*a*,*b*). Similar to the TKE spectra, the figure shows a monotonic increase with the Reynolds number and a decrease with the specific gas constant. A similar dependence on *Re* and *R* implies a close relation

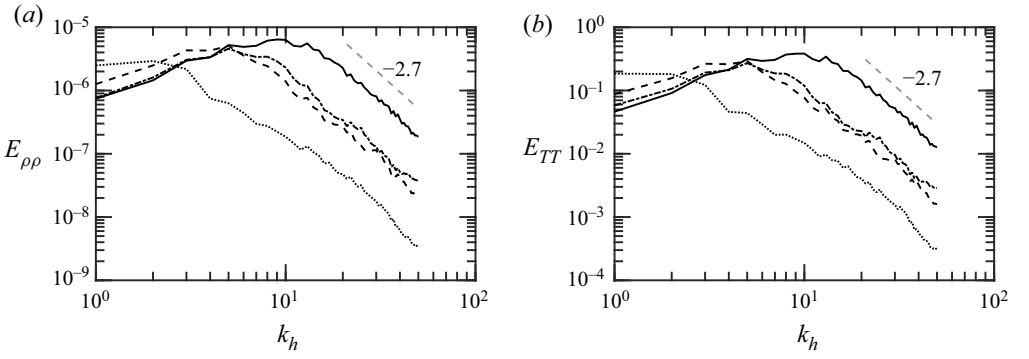

Figure 19. Spectra of (*a*) density and (*b*) temperature from thermal plume (case 5) at $z \approx 2D$ (solid), $z \approx 3D$ (dashed), $z \approx 5D$ (dash-dotted) and $z \approx 10D$ (dotted).

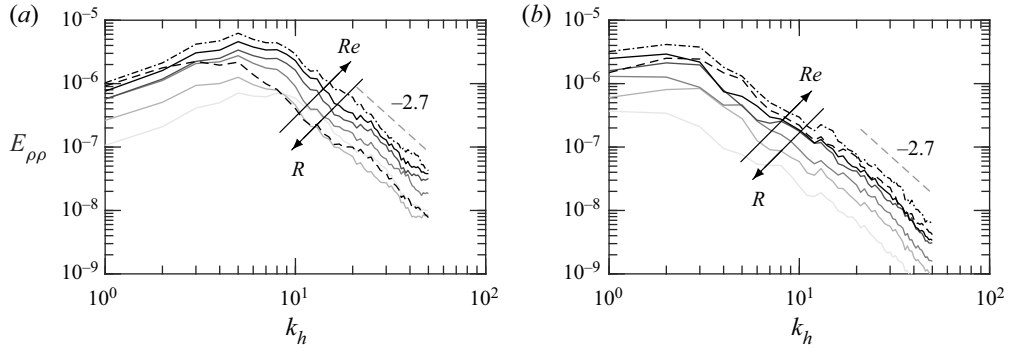

Figure 20. Density spectra from thermal (grey, solid), methane (black dashed) and sulphur dioxide plumes (black dash-dotted) at (*a*) $z \approx 5D$ and (*b*) $z \approx 10D$. Same colours and lines as in figure 3.

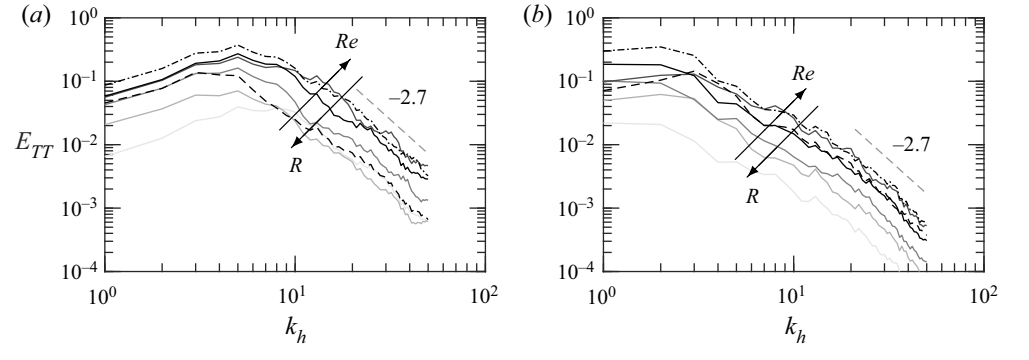

Figure 21. Temperature spectra from thermal (grey, solid), methane (black dashed) and sulphur dioxide plumes (black dash-dotted) at (*a*) $z \approx 5D$ and (*b*) $z \approx 10D$. Same colours and lines as in figure 3.

between velocities and thermodynamic variables. A possible correlation will be discussed by examining the turbulent mass and heat fluxes, $\overline{\rho' u_i''}$ and $\widetilde{T' u_i''}$ in the following section.

The LES work of Chen & Bhaganagar (2021) has shown that, for thermal plumes, the baroclinic terms are the most important mechanisms that contribute to the

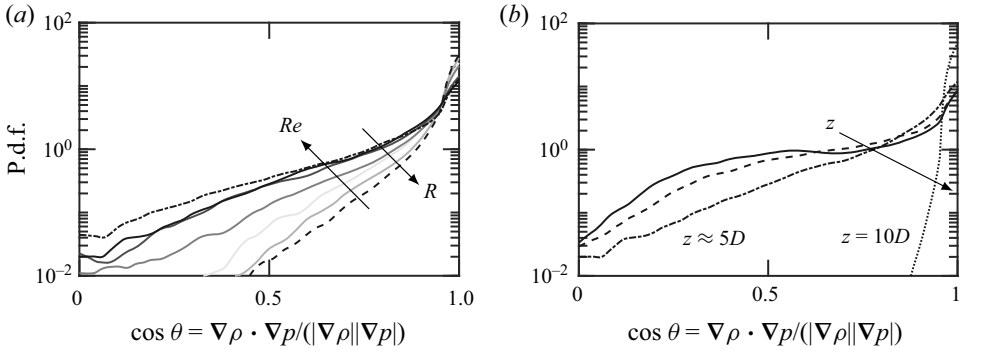

Figure 22. Cosine angle between the density and pressure gradients of (*a*) thermal (solid), methane (dashed) and sulphur dioxide (dash-dotted) plumes at $z \approx 5D$ and (*b*) thermal plumes at $z \approx 2D$ (solid) $z \approx 3D$ (dashed) $z \approx 5D$ (dash-dotted) $z \approx 10D$ (dotted). Same grey lines as in figure 3.

vorticity dynamics. To further understand how the misalignment between density and pressure changes across the plumes, figure 22 shows the probability distribution function (p.d.f.) of the cosine angle between $\nabla\rho$ and ∇p. In figure 22(*a*), the p.d.f.s of different species and heat sources at $z/D \approx 5$ are presented. The angle between $\nabla\rho$ and ∇p increases with Reynolds number. On the other hand, an opposite trend is found with the specific gas constant. The density gradients become more aligned with pressure gradients for buoyant plumes. The change implies that the vorticity intensity is reduced when lighter gases are released into the plumes. Such a change indicates a possible weaker turbulent mixing. The p.d.f.s of $\nabla\rho\cdot\nabla p$ in thermal plumes at different heights are plotted in figure 22(*b*). With the ascending plumes, the cosine angle shows a clear decrease. However, the decrease in the initial stage ($z/D \leqslant 5$) is minor. When the plumes enter the mixing stage ($z/D > 5$), the angles are reduced significantly. The significant reduction of the misalignment not only points out the decrease in vorticity, but it also implies the change in the turbulent structures, as substantial transverse evolution occurs.

5. Cross-correlations between velocity, density and temperature

5.1. *Turbulent mass fluxes*

In buoyant, variable-density flows, the mean scalar equation (density and temperature) contains turbulent scalar flux and turbulent heat flux terms, and the budget of these terms will provide guidance on the dominant mechanisms that control the correlations between the scalars and the velocity. Based on the analysis of the Reynolds stress transport terms and the variances of temperature and density, a similarity between the two suggests a strong correlation between velocity and thermodynamic variables. We next discuss the budgets of turbulent mass flux ($\overline{\rho' u_i''}$) and turbulent heat flux ($\widetilde{T'' u_i''}$).

The spatial evolution of turbulent mass fluxes along the centreline is plotted in figure 23(*a*,*b*). Both the axial and horizontal components are normalized by the root mean square of the corresponding velocity and density fluctuations. The horizontal mass fluxes fluctuate around zero along the centreline in thermal plumes, revealing a negligible connection between ρ' and u''. However, the mass fluxes in methane and sulphur dioxide plumes show a minor correlation, which is due to the density difference between the air and the species. On the contrary, a near perfect anti-correlation is observed between ρ'

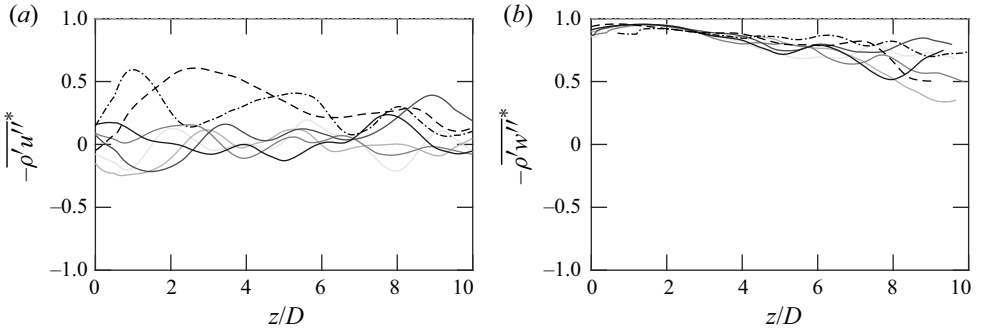

Figure 23. Centreline distributions of $\overline{\rho' u''}^*$ $(=\overline{\rho' u''}/(\sqrt{\overline{\rho'^2}}\sqrt{\widetilde{u''^2}})$ and $\overline{\rho' w''}^*$ $(=\overline{\rho' w''}/(\sqrt{\overline{\rho'^2}}\sqrt{\widetilde{w''^2}}))$.

and w''. The negative correlation can be explained as due to mass conservation. The axial fluxes are very close to unity near the source and slowly decrease with height. However, the correlations are still above 0.5 even at $z = 10D$. The evolution of $\overline{\rho' w''}$ indicates that density fluctuations are highly correlated with the axial Reynolds stress rather than with the horizontal velocity.

The budget analyses of the Reynolds stress and thermodynamic variances have shown that multiple mechanisms control the spatial development of density and the Reynolds stresses. To understand the mechanisms involved in the correlations of these two variables, the budget terms of turbulent mass fluxes are computed

$$\frac{\partial \widetilde{u}_j \overline{\rho' u_i''}}{\partial x_j} = B_\rho + \mathcal{P}_{\rho u} + P_{\rho u} + \Pi_{\rho u} + \Phi_\rho + \epsilon_{\rho u} + \mathcal{T}_{\rho u}. \tag{5.1}$$

The turbulent mass-flux equation is governed by similar processes as the Reynolds stress equation. The term on the left-hand side is the convection term and it represents the spatial variation of the density and velocity correlation. The convection term is balanced by the terms on the right-hand side. These terms include the buoyancy B_ρ, production $\mathcal{P}_{\rho u}$ and $P_{\rho u}$, dilatation $\Pi_{\rho u}$, pressure distribution $\Phi_{\rho u}$, dissipation $\epsilon_{\rho u}$ and transport $\mathcal{T}_{\rho u}$. The mathematical form of those terms is given as

$$B_\rho = -\frac{\overline{\rho'^2}}{\bar{\rho}} g_i \tag{5.2a}$$

$$\mathcal{P}_{\rho u} = \overline{\rho' u_j''} \frac{\partial \widetilde{u}_i}{\partial x_j} + \frac{\overline{\rho'^2}}{\bar{\rho}} \frac{\partial \overline{\sigma_{ij}}}{\partial x_j} \tag{5.2b}$$

$$P_{\rho u} = -R_{ij} \frac{\partial \bar{\rho}}{\partial x_j} \tag{5.2c}$$

$$\Pi_{\rho u} = -\bar{\rho} \overline{u_i'' \frac{\partial u_j''}{\partial x_j}} \tag{5.2d}$$

$$\Phi_\rho = \frac{1}{\bar{\rho}} \overline{p' \frac{\partial \rho'}{\partial x_i}} \tag{5.2e}$$

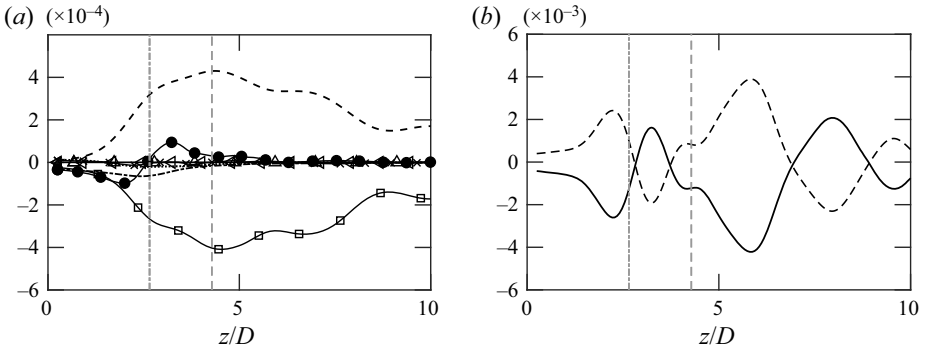

Figure 24. (*a*) Distributions of $\overline{\rho' u_3''}$ budget terms from case 5: convection (•); B_ρ (−·); $\mathcal{P}_{\rho u}$ (···); $P_{\rho u}$ (−−); $\Pi_{\rho u}$ (□); Φ_ρ (◁); $\epsilon_{\rho u}$ (△); $\mathcal{T}_{\rho u}$ (×). (*b*) Distributions of vertical (−) and horizontal (−−) components of $\Pi_{\rho u}$. Vertical grey lines: $\overline{\rho' w''}_{max}$ (dash-dotted) and $R_{33,max}$ (dashed).

$$\epsilon_{\rho u} = -\frac{1}{\bar{\rho}}\overline{\sigma'_{ij}\frac{\partial \rho'}{\partial x_j}} \tag{5.2f}$$

$$\mathcal{T}_{\rho u} = -\frac{1}{\bar{\rho}}\overline{\frac{\partial \rho' p'}{\partial x_i}} + \frac{1}{\bar{\rho}}\overline{\frac{\partial \rho' \sigma'_{ij}}{\partial x_j}} - \frac{1}{\bar{\rho}}\frac{\partial}{\partial x_j}\overline{\frac{\rho' u_i'' u_j''}{\bar{\rho}}}. \tag{5.2g}$$

The budget terms of $\overline{\rho' w''}$ are plotted in figure 24(*a*). The dominant terms in the evolution of $\overline{\rho' w''}$ are $P_{\rho u}$ and $\Pi_{\rho u}$. This is consistent with the budget analysis of $\overline{\rho'^2}$ in which axial dilatation and the density gradient are the main mechanisms. However, dilatational effects become negative and production becomes positive to the mass-flux transport. During the initial plume development stage, $\Pi_{\rho u}$ has a monotonic increase. As the flow enters the mixing stage, $\Pi_{\rho u}$ starts decreasing. The decomposition of $\Pi_{\rho u}$ is shown in figure 24(*b*), in which the term is decomposed into horizontal and vertical components. The two components show opposite signs throughout the plumes. Unlike the main mechanisms in velocity and density, the dominant terms in $\overline{\rho' w''}$ peak at $z/D \approx 5$ where $R_{33,max}$ occurs.

5.2. *Turbulent heat fluxes*

Besides the turbulent mass fluxes, the correlation between temperature and the velocities can be realized through turbulent heat fluxes. Figure 25(*a*,*b*) shows the distributions of $\widetilde{T'' u''}$ and $\widetilde{T'' w''}$ normalized by the corresponding root-mean-square temperature and velocities. Similar to horizontal mass fluxes, a very weak connection can be seen between temperature and horizontal velocities in thermal plumes as the horizontal heat fluctuates around zero. A minor correlation exists in the plumes with methane and sulphur dioxide. In contrast, the correlations of temperature and the vertical velocities show a perfect anti-correlation near the source and slowly decrease as the plume rises. Similar to density, the turbulent heat fluxes show that temperature fluctuations are strongly associated with the axial motions.

As the correlation between temperature and the velocities exists, it is necessary to identify the mechanisms that control the correlations. The budget terms of the turbulent

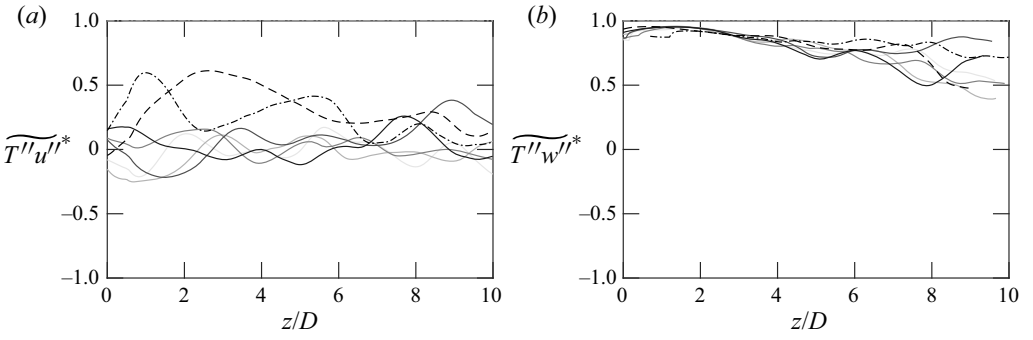

Figure 25. Centreline distributions of $\widetilde{T''u''}^*$ $(=\widetilde{T''u''}/(\sqrt{\widetilde{T''^2}}\sqrt{\widetilde{u''^2}})$ and $\widetilde{T''w''}^*$ $(=\widetilde{T''w''}/(\sqrt{\widetilde{T''^2}}\sqrt{\widetilde{w''^2}}))$.

heat fluxes are computed

$$\bar{\rho}\tilde{u}_j\frac{\partial\widetilde{T''u_i''}}{\partial x_j} = B_T + \mathcal{P}_{Tu} + P_{Tu} + \Pi_{Tu} + \Phi_T + \epsilon_{Tu} + \mathcal{T}_{Tu}. \tag{5.3}$$

Similar to the mass fluxes, the spatial development of turbulent heat flux is controlled by a balance of the terms on the right. The first three terms on the right are the productions due to buoyancy (B_T), mean flows ($\mathcal{P}_{Tu}$) and the temperature gradient (P_{Tu}). The following two terms are contributions from dilatation (Π_{Tu}) and pressure distribution (Φ_{Tu}). Finally, the last two terms are dissipation (ϵ_{Tu}) and transport ($\mathcal{T}_{Tu}$). The explicit form of each term is given as follows:

$$B_T = -\overline{\rho' T''}g_i \tag{5.4a}$$

$$\mathcal{P}_{Tu} = -\bar{\rho}\widetilde{T''u_j''}\frac{\partial\tilde{u}_i}{\partial x_j} - \frac{1}{C_v}\overline{pu_i''}\frac{\partial\tilde{u}_j}{\partial x_j} + \frac{1}{C_v}\overline{\sigma_{jk}u_i''}\frac{\partial\tilde{u}_j}{\partial x_k} \tag{5.4b}$$

$$P_{Tu} = -\bar{\rho}R_{ij}\frac{\partial\tilde{T}}{\partial x_j} \tag{5.4c}$$

$$\Pi_{Tu} = -\frac{1}{C_v}\overline{pu_i''\frac{\partial u_j''}{\partial x_j}} \tag{5.4d}$$

$$\Phi_T = \overline{p'\frac{\partial T''}{\partial x_i}} \tag{5.4e}$$

$$\epsilon_{Tu} = \frac{1}{C_v}\overline{\sigma_{jk}u_i''\frac{\partial u_j''}{\partial x_k}} - \overline{\sigma_{ij}\frac{\partial T''}{\partial x_j}} - \frac{1}{C_v}\overline{k_T\frac{\partial u_i''}{\partial x_j}\frac{\partial T}{\partial x_j}} \tag{5.4f}$$

$$\mathcal{T}_{Tu} = -\frac{\partial\overline{\rho T''u_j''u_i''}}{\partial x_j} - \frac{\partial\overline{p'T''}}{\partial x_i} + \frac{\partial\overline{\sigma_{ij}T''}}{\partial x_j} + \frac{1}{C_v}\frac{\partial}{\partial x_j}\overline{k_T u_i''\frac{\partial T}{\partial x_j}}. \tag{5.4g}$$

Here, ϵ contains both viscous and thermal dissipation and $\mathcal{T}_{Tu}$ includes turbulent, pressure, viscous and thermal transport.

The budget terms of turbulent heat fluxes are plotted in figure 26(*a*). The figure shows that the dominant terms for axial heat fluxes are the production of mean flow and dilatational motions. Similar to $\overline{\rho' w''}$, both the dominant terms of $\widetilde{T''w''}$ have a

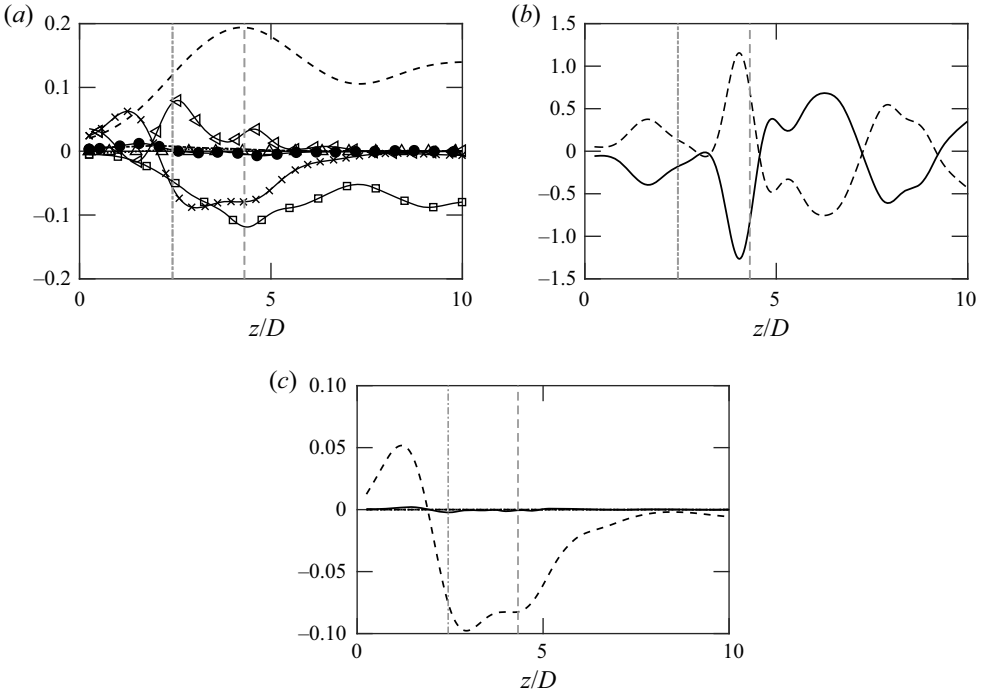

Figure 26. (*a*) Distributions of $\widetilde{T''w''}$ budget terms from case 5: convection (•), B_T (−·); $\mathcal{P}_{Tu}$ (· · ·); P_{Tu} (−−); Π_{Tu} (□); Φ_T (◁); ϵ_{Tu} (Δ); $\mathcal{T}_{Tu}$ (×). (*b*) Distributions of vertical (−) and horizontal (−−) components of Π_{Tu}. (*c*) Distributions of transport terms: $\partial_z\overline{\rho T''w''^2}$ (−); $\partial_z\overline{p'T''}$ (−−); $\partial_z\overline{\sigma_{33}T''}$ (−·); $\partial_z\overline{k_T w''^2}\partial_z T$ (· · ·). Vertical grey lines: $\widetilde{T''w''}_{max}$ (dash-dotted) and $R_{33,max}$ (dashed).

monotonic increase in the initial stage and peak at $R_{33,max}$. As the plume enters the mixing stage, the two mechanisms slowly decrease. The dilatation can be further decomposed into vertical and horizontal motions. Figure 26(*b*) shows that the two components have opposite distributions and counteract each other. In contrast to Reynolds stresses and thermodynamic variances, both the dilatational effects of $\overline{\rho'w''}$ and $\widetilde{T''w''}$ reach their maximum near $z/D = 5$ at which the anisotropic phenomenon is weak. This observation seems to suggest that $\Pi_{\rho u}$ and Π_{Tu} have a strong dependence on w'' rather than on the density. More details will be presented in the following discussion. Besides the production and dilatation, the pressure distribution and pressure transport (from figure 26*c*) are also important. Unlike $\overline{\rho'^2}$, $\widetilde{T''^2}$ and $\overline{\rho'w''}$ which are only dependent on production and dilatation, the additional terms involved in the transport of $\widetilde{T''w''}$ indicate a more complicated correlation between temperature and velocity. Further investigations will be conducted in future work.

Finally, we present the budget terms of $\overline{\rho'w''}$ and $\widetilde{T''w''}$ at $z/D = 5$ where the variables peak in figure 27. Consistent with the centreline distributions, the radial transport of $\overline{\rho'w''}$ is still dominated by $P_{\rho u}$ and $\Pi_{\rho u}$. For $\widetilde{T''w''}$, the main terms are P_{Tu}, Π_{Tu}, Φ_T and $\mathcal{T}_{Tu}$. Despite the distance from the source, the figure shows that turbulent motions mostly occur within $x/D < 0.5$.

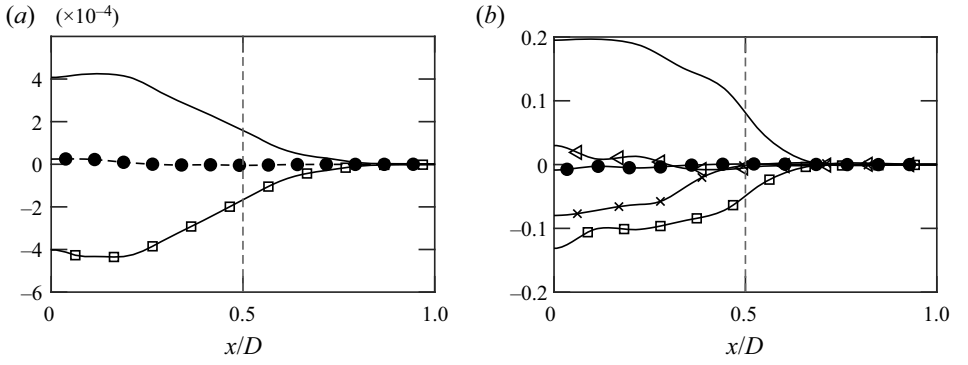

Figure 27. (*a*) Radial profiles of $\overline{\rho' w''}$ budgets at $z/D \approx 5$: $\partial_j(\widetilde{u}_j\overline{\rho' w''})$ (•); $P_{\rho u}$ (−−) and $\Pi_{\rho u}$ (□). (*b*) Radial profiles of $\widetilde{T''w''}$ budgets at the same heights: $\bar{\rho}\widetilde{u}_j\partial_j\widetilde{T''w''}$ (•); P_{Tu} (lines), Π_{Tu} (□), Φ_T (◁) and $\mathcal{T}_{Tu}$ (×).

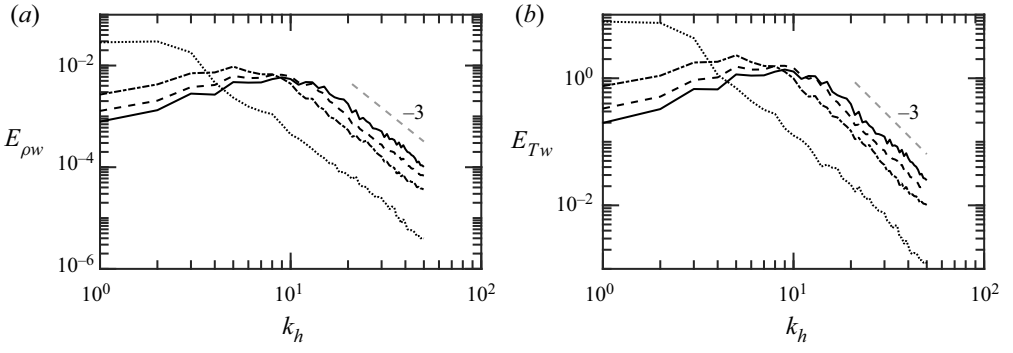

Figure 28. Spectra of (*a*) ρu and (*b*) Tw from thermal plume at $z \approx 2D$ (solid), $z \approx 3D$ (dashed), $z \approx 5D$ (dash-dotted) and $z \approx 10D$ (dotted). Same colours and lines as figure 19.

5.3. *Spectra and characteristic scales*

Turbulent fluctuations exist in a wide range of scales. As the axial dilatation is identified as being the mechanism that contributes to thermodynamic fluctuations in the buoyant plumes, it is important to identity the scales at which the interaction occurs. We plot the spectra of the axial mass and heat fluxes in figure 28(*a*,*b*). The spectra are compared at multiple different heights. The figure shows that the thermodynamic variables are correlated with velocity at large scales. In addition, the spectra of the correlation resemble the energy spectra of vertical velocity. The buoyancy range with −3 slope is observed in both fluxes at different heights. The observed −3, instead of −2.7, slope confirms that the velocities are dominant over the thermodynamic fluctuations in the correlation term. The similarity between E_{ww}, $E_{\rho w}$ and E_{Tw} indicates that the correlation is influenced by velocity fluctuations rather than the thermodynamic variables.

The present work has shown that vertical velocity strongly correlates with density and temperature. From the spectra, we realize that these correlations are mostly influenced by velocity fluctuations. To further understand the related temporal characteristics, we present the characteristic time scales (Skamarock *et al.* 2014)

$$\tau = k^{-3/2}E(k)^{-1/2} \tag{5.5}$$

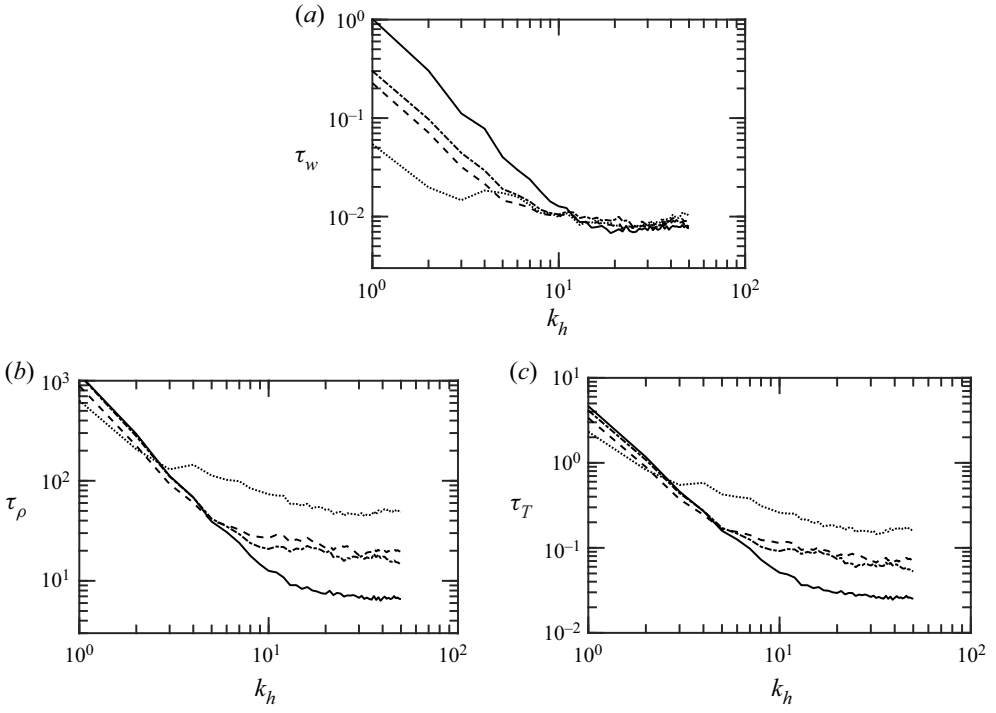

Figure 29. Characteristic time scales from the spectra of (*a*) vertical velocity (w''), (*b*) density (ρ') and (*c*) temperature (T'') at $z/D \approx 2$ (solid), $z/D \approx 3$ (dashed), $z/D \approx 5$ (dash-dotted) and $z/D \approx 10$ (dotted).

in figure 29. From (5.5), $\tau(k)$ represents the characteristic time in synoptic scale, which corresponds to the buoyancy range. The characteristic time scale of vertical velocity, τ_w, reaches an asymptotic state in the buoyancy regime and such an observation is consistent with other studies (Skamarock *et al.* 2014). Further, this asymptotic condition is invariant with plume height. On the other hand, although the time scales for density and temperature also asymptote at higher wavenumbers, the asymptotic value increases with increasing plume height. The comparison of the time scales τ_w, τ_ρ and τ_T suggest that the turnover time scales of velocity are much smaller than the thermodynamic variables.

The present study focused on the mechanisms for the evolution of Reynolds stresses and thermodynamic fluctuations for active scalar mixing. The thermodynamic fluctuations are attributed to the axial dilatation at large scales. In isotropic turbulence, thermodynamic spectra mostly show a spectral slope $\approx -7/3$ at the intermediate scales. On the contrary, such a slope is not found in the present work. The thermodynamic spectra show a value of -2.7, which is similar with the studies of stratified turbulence (Carnevale *et al.* 2001; Waite 2011). Since buoyancy was found to be negligible in the cross-relations of velocity and thermodynamic variables, the change of spectral slope from isotropic turbulence is an interesting and important discovery.

6. Conclusions

Using the LES database, we studied the scaling, budget and spectra of turbulent kinetic energy, thermodynamic variables and their cross-relations for turbulent buoyant plumes. To assess the generality of the fundamental investigations, heat sources with a range

of thermal flux conditions were presented. The different heat fluxes result in different values of the Reynolds number, and the effects of released heat are discussed in terms of dimensionless numbers. In addition to thermal plumes, additional cases of heated methane and heated sulphur dioxide released from the source were also included in the study for a comprehensive discussion. To account for the compressible nature, Favre averaging was implemented. Two distinct stages, initial and mixing, were shown characterizing the evolution of both velocity and thermodynamic fluctuations. Multiple mechanisms were found to be attributed to TKE generation. The velocity fluctuations further contributed to thermodynamic fluctuations, and the mechanisms that control the processes were identified.

In the present work, it has been identified that the Reynolds stresses decay exponentially with an exponent of -1 along the centreline during the mixing stage. The ratio of vertical to horizontal stresses (R_{33} and R_{11}) shows a strong anisotropy near the source. However, the turbulence slowly approaches an isotropic state during the mixing stage. The discoveries are consistent among thermal, methane and sulphur dioxide plumes. Budget analysis shows that R_{33} is dominated by multiple terms, including buoyancy and mean-flow production, dilatation and transport. The buoyant production dominates during the initial stage, while the mean-flow production becomes important during the mixing stage. The buoyant production shows a monotonic increase in magnitude with Re for thermal plumes. Comparing with heated gas plumes with the same heat source, the buoyant contribution becomes stronger for heavier species and it peaks closer to the source. For R_{11}, only dilatational contributions and dissipation are found to be important. The existence of a buoyancy regime has been identified for both thermal and gas plumes. The energy spectra for both axial and horizontal velocity components show a -3 spectral slope at different heights. Lighter gas plumes have higher energy intensities at different heights compared with the thermal plumes.

We have also studied the thermodynamic variables, particularly density and temperature. The variances of both the variables reach their peak near $z/D = 3$ and the values normalized by their maximum shows a scaling with an exponent of -2.5. When density and temperature fluctuations are normalized by their local averages, the obtained scaling shows a consistent -2.3 exponent for different plumes. In addition, the normalized quantities increase with Re but decrease with R (gas constant). Budget analysis of the variances of density and temperature shows that both the quantities are strongly dependent on the axial dilatation motions and the production of thermodynamic gradients. The strong correlation between the axial velocity and the density (and temperature) fluctuations is the main dominating mechanism in the thermodynamic variance equation. The spectra of density and temperature have a -2.7 slope at the intermediate scales with a systematic dependence on Re and R. Within the plumes, the angles between pressure and density gradients increase with Re but decrease with R. During the initial stage, the changes of such angles are very minor. However, the misalignment between pressure and density decreases significantly with height in the mixing stage. The drastic changes may have clear impacts on turbulent mixing and energy dissipation, which will be further studied in the future.

To have a complete discussion on thermodynamic variables, cross-correlations between velocity and thermodynamic variables are also discussed. The cross-correlations between horizontal velocity and thermodynamic quantities are extremely weak for thermal plumes. However, minor correlations exist for methane and sulphur dioxide plumes. On the contrary, a strong correlation exists between the axial velocity fluctuations and both the density and the temperature fluctuations. It has been confirmed from the budget analysis

that thermodynamic fluctuations are generated by the axial velocity through dilatational motions (correlation between the velocity and thermodynamic fluctuation).

Despite the existence of turbulence production in $\overline{\rho' w''}$ and $\widetilde{T'' w''}$, these two terms are negligible. Finally, the spectra of the $\overline{\rho' w''}$ and $\widetilde{T'' w''}$ show that thermodynamic variables are correlated with the velocity at large scales. With a clear buoyancy slope (-3), the spectra further indicate that both the turbulent fluxes have a strong influence of the velocity rather than the thermodynamic quantities. Finally, the time scale of the vertical velocity obtained from the spectra reaches an asymptotic state in the buoyancy regime, which is an indication that turbulent fluctuations have been captured quantitatively.

Our investigations reveal the fundamental structures of velocities and thermodynamic fluctuations in turbulent buoyant plumes. The results provide a guidance on the important mechanisms that govern the turbulence velocity and thermodynamic processes which are important to engineering applications and environmental predictions. The present work has important implications in developing turbulent models to simulate plumes at very high Reynolds number. By accounting for the density effects and the correlation between the velocity and the thermodynamics fields, realistic turbulence can be realized. We acknowledge that some extreme events in turbulence which occur at small scales are not captured in turbulence models. However, the presented spectra show that the discussed phenomena mostly happen at large scales. The present work on the fundamental aspects of turbulence generated in a buoyant plume with a detailed discussion of energy transfer and thermodynamic structures within turbulent buoyant plumes is an important contribution to buoyant convection studies.

The work has important implications for entrainment modelling in plumes. The present study indicates the entrainment modelling should account for the correlations between the scalar density field and the velocity fields. The mean scalar equation contains the turbulent scalar heat flux and turbulence scalar flux terms which are due to the production of turbulent mass flux/heat flux and axial dilatation. The radial transport of the axial heat flux is dominated by these effects, which suggests a relation of the correlations between the velocity and thermodynamics that influences the entrainment processes. Future work will focus on modifying the existing theoretical formulations on entrainment using the framework that has been developed in this study.

Acknowledgements. The authors would like to acknowledge Texas Advanced Computing Center (TACC) for computational resources and NASA for financial support. The authors acknowledge Sudheer BhimiReddy and J. Slaten, graduate students in the Laboratory of Turbulence and Sensing at University of Texas, San Antonio, who have helped with conducting the simulations to generate the LES data. K.B. acknowledges various stimulating discussions with Dr Bill George on this topic. The authors thank graduate student Thanh Tran for helping with the visual for the graphical abstract.

Funding. Funding for the study was obtained from NASA Center for Advanced Measurements in Extreme Environments, Grant No. 80NSSC19M019.

Declaration of interests. The authors report no conflict of interest.

Data availability statement. The data presented in this work are available from the corresponding author on reasonable request.

Author ORCIDs.
Chang Hsin Chen https://orcid.org/0000-0002-7862-2702;
Kiran Bhaganagar https://orcid.org/0000-0001-5205-4690.

Author contributions. Both the authors contributed equally to analysing data and reaching conclusions, and in writing the paper.

Appendix A. Transport equation of Reynolds stresses

The mathematical derivation of (3.1) is presented in this section as a reference. The equation of Reynolds stresses is obtained from Navier–Stokes equations

$$\frac{\partial \rho u_i}{\partial t} + \frac{\partial \rho u_j u_i}{\partial x_j} = -\frac{\partial p}{\partial x_i} + \frac{\partial \sigma_{ij}}{\partial x_j} - \rho g_i. \tag{A1}$$

By taking the Reynolds averaging of (A1), we have

$$\frac{\partial \bar{\rho}\widetilde{u_i}}{\partial t} + \frac{\partial \bar{\rho}\widetilde{u_j}\widetilde{u_i} + \bar{\rho}R_{ij}}{\partial x_j} = -\frac{\partial \bar{p}}{\partial x_i} + \frac{\partial \bar{\sigma}_{ij}}{\partial x_j} - \bar{\rho} g_i. \tag{A2}$$

Subtracting (A2) from (A1) yields $\rho u_i''$

$$\rho\frac{\partial u_i''}{\partial t} + \rho\tilde{u}_j\frac{\partial u_i''}{\partial x_j} + \rho u_j''\frac{\partial \tilde{u}_i}{\partial x_j} + \rho u_j''\frac{\partial u_i''}{\partial x_j} = -\frac{\partial p'}{\partial x_i} + \frac{\partial \sigma_{ij}'}{\partial x_j} + \frac{\partial \bar{\rho}R_{ij}}{\partial x_j} + \frac{\rho'}{\bar{\rho}}\left[\frac{\partial \bar{p}}{\partial x_i} - \frac{\partial \overline{\sigma_{ij}}}{\partial x_j} + \frac{\partial \bar{\rho}R_{ij}}{\partial x_j}\right] - \bar{\rho} g_i. \tag{A3}$$

The equation for the Reynolds stresses is, therefore, generated by averaging the product of u_j'' with the equation for $\rho u_i''$, and summing with the average of the product of u_i'' with the equation for $\rho u_j''$. Finally, (3.1) is formed by implementing the hydrostatic condition ($\partial_\alpha \bar{p} = -\bar{\rho} g_\alpha$)

$$\bar{\rho}\frac{\partial R_{\alpha\alpha}}{\partial t} + \bar{\rho}\tilde{u}_k\frac{\partial R_{\alpha\alpha}}{\partial x_k} = -2\overline{\rho' u_\alpha''}g_\alpha - 2\bar{\rho}R_{\alpha k}\frac{\partial \tilde{u}_\alpha}{\partial x_k} + 2\overline{p'\frac{\partial u_\alpha''}{\partial x_\alpha}} - 2\overline{\sigma_{\alpha k}'\frac{\partial u_\alpha''}{\partial x_k}} + 2\overline{u_\alpha''}\frac{\partial \overline{\sigma_{\alpha k}}}{\partial x_k} - \frac{\partial \bar{\rho}\overline{u_\alpha'' u_\alpha'' u_k''}}{\partial x_k} - 2\frac{\partial \overline{p' u_\alpha''}}{\partial x_\alpha} + 2\frac{\partial \overline{\sigma_{\alpha k}' u_\alpha''}}{\partial x_k}. \tag{A4}$$

For stationary turbulent flows, the transient term can be dropped. A similar method can also be applied to obtain the equation for $\overline{\rho'^2}$, $\widetilde{T''^2}$, $\overline{\rho' u_i''}$ and $\widetilde{T'' u_i''}$.

References

Adkins, J.F., McIntyre, K. & Schrag, D.P. 2002 The salinity, temperature, and δ^{18}O of the glacial deep ocean. *Science* **298** (5599), 1769–1773.

Ai, J., Law, A.W.-K. & Yu, S.C.M. 2006 On Boussinesq and non-Boussinesq starting forced plumes. *J. Fluid Mech.* **558**, 357–386.

Amielh, M., Djeridane, T., Anselmet, F. & Fulachier, L. 1996 Velocity near-field of variable density turbulent jets. *Intl J. Heat Mass Transfer* **39** (10), 2149–2164.

Bastiaans, R.J.M., Rindt, C.C.M., Nieuwstadt, F.T.M. & Steenhoven, A.A. 2000 Direct and large-eddy simulation of the transition of two- and three-dimensional plane plumes in a confined enclosure. *Int. J. Heat Mass Transf.* **43** (13), 2375–2393.

Batchelor, G.K. 1954 Heat convection and buoyancy effects in fluids. *Q. J. R. Meteorol. Soc.* **80** (345), 339–358.

Bhaganagar, K. & Bhimireddy, S.R. 2017 Assessment of the plume dispersion due to chemical attack on April 4, 2017, in Syria. *Nat. Hazards* **88** (3), 1893–1901.

Bhaganagar, K. & Bhimireddy, S.R. 2020*a* Local atmospheric factors that enhance air-borne dispersion of coronavirus-high-fidelity numerical simulation of COVID19 case study in real-time. *Environ. Res.* **191**, 110170.

Bhaganagar, K. & Bhimireddy, S.R. 2020*b* Numerical investigation of starting turbulent buoyant plumes released in neutral atmosphere. *J. Fluid Mech.* **900**, A32.

BHAMIDIPATI, N. & WOODS, A.W. 2017 On the dynamics of starting plumes. *J. Fluid Mech.* **833**, R2.
BHIMIREDDY, S.R. & BHAGANAGAR, K. 2018*a* Performance assessment of dynamic downscaling of WRF to simulate convective conditions during sagebrush phase 1 tracer experiments. *Atmosphere* **9** (12), 505.
BHIMIREDDY, S.R. & BHAGANAGAR, K. 2018*b* Short-term passive tracer plume dispersion in convective boundary layer using a high-resolution WRF-ARW model. *Atmos. Pollut. Res.* **9** (5), 901–911.
BHIMIREDDY, S.R. & BHAGANAGAR, K. 2021 Implementing a new formulation in WRF-LES for buoyant plume simulations: bPlume-WRF-LES model. *Mon. Weath. Rev.* **149** (7), 2299–2319.
BILLANT, P. & CHOMAZ, J.-M. 2001 Self-similarity of strongly stratified inviscid flows. *Phys. Fluids* **13** (6), 1645–1651.
CARNEVALE, G.F., BRISCOLINI, M. & ORLANDI, P. 2001 Buoyancy- to inertial-range transition in forced stratified turbulence. *J. Fluid Mech.* **427**, 205–239.
CHARONKO, J.J. & PRESTRIDGE, K. 2017 Variable-density mixing in turbulent jets with coflow. *J. Fluid Mech.* **825**, 887–921.
CHASSAING, P., HARRAN, G. & JOLY, L. 1994 Density fluctuation correlations in free turbulent binary mixing. *J. Fluid Mech.* **279**, 239–278.
CHEN, C.H. & BHAGANAGAR, K. 2021 New findings in vorticity dynamics of turbulent buoyant plumes. *Phys. Fluids* **33** (11), 115104.
CHEN, C.J. & RODI, W. 1980 Vertical turbulent buoyant jets: a review of experimental data. NASA STI/Recon Technical Report A, 80:23073.
CORRSIN, S. 1951 On the spectrum of isotropic temperature fluctuations in an isotropic turbulence. *J. Appl. Phys.* **22** (4), 469–473.
DARISSE, A., LEMAY, J. & BENAÏSSA, A. 2015 Budgets of turbulent kinetic energy, Reynolds stresses, variance of temperature fluctuations and turbulent heat fluxes in a round jet. *J. Fluid Mech.* **774**, 95–142.
DEVENISH, B.J., ROONEY, G.G. & THOMSON, D.J. 2010 Large-eddy simulation of a buoyant plume in uniform and stably stratified environments. *J. Fluid Mech.* **652**, 75–103.
DIMOTAKIS, P.E. 2005 Turbulent mixing. *Annu. Rev. Fluid Mech.* **37** (1), 329–356.
DJERIDANE, T., AMIELH, M., ANSELMET, F. & FULACHIER, L. 1996 Velocity turbulence properties in the near-field region of axisymmetric variable density jets. *Phys. Fluids* **8** (6), 1614–1630.
DONZIS, D.A. & JAGANNATHAN, S. 2013 Fluctuations of thermodynamic variables in stationary compressible turbulence. *J. Fluid Mech.* **733**, 221–244.
DONZIS, D.A. & JOHN PANICKACHERIL, J. 2020 Universality and scaling in homogeneous compressible turbulence. *Phys. Rev. Fluids* **5**, 084609.
EZZAMEL, A., SALIZZONI, P. & HUNT, G.R. 2015 Dynamical variability of axisymmetric buoyant plumes. *J. Fluid Mech.* **765**, 576–611.
GOULDIN, F.C., SCHEFER, R.W., JOHNSON, S.C. & KOLLMANN, W. 1986 Nonreacting turbulent mixing flows. *Prog. Energy Combust. Sci.* **12** (4), 257–303.
JEONG, J. & HUSSAIN, F. 1995 On the Identification of a Vortex. *J. Fluid Mech.* **285**, 69–94.
KOLMOGOROV, A.N. 1941 Local structure of turbulence in an incompressible fluid for very large Reynolds numbers. *Dokl. Akad. Nauk SSSR* **30**, 299–303.
LINDBORG, E. 2006 The energy cascade in a strongly stratified fluid. *J. Fluid Mech.* **550**, 207–242.
LUMLEY, J.L. 1964 The spectrum of nearly inertial turbulence in a stably stratified fluid. *J. Atmos. Sci.* **21**, 99–102.
LUMLEY, J.L. & PANOFSKY, H.A. 1965 The structure of atmospheric turbulence. *Quarterly J. R. Meteorol. Soc.* **91** (389), 400.
LUO, T., WANG, J., XIE, C., WAN, M. & CHEN, S. 2020 Effects of compressibility and Atwood number on the single-mode Rayleigh–Taylor instability. *Phys. Fluids* **32** (1), 012110.
MESHKOV, E.E. 1969 Instability of the interface of two gases accelerated by a shock wave. *Fluid Dyn.* **4**, 101–104.
MORTON, B.R., TAYLOR, G.I. & TURNER, J.S. 1956 Turbulent gravitational convection from maintained and instantaneous sources. *Proc. R. Soc. Lond.* A **234** (1196), 1–23.
NIEUWSTADT, F.T.M. & DE VALK, J.P.J.M.M. 1987 A large eddy simulation of buoyant and non-buoyant plume dispersion in the atmospheric boundary layer. *Atmos. Environ.* **21** (12), 2573–2587.
OBUKHOV, A.M. 1949 The structure of the temperature field in a turbulent flow. *Izv. Akad. Nauk. SSSR* **13**, 58–69.
O'HERN, T.J., WECKMAN, E.J., GERHART, A.L., TIESZEN, S.R. & SCHEFER, R.W. 2005 Experimental study of a turbulent buoyant helium plume. *J. Fluid Mech.* **544**, 143–171.
PANCHAPAKESAN, N.R. & LUMLEY, J.L. 1993 Turbulence measurements in axisymmetric jets of air and helium. Part 1. Air jet. *J. Fluid Mech.* **246**, 197–223.

PAPANICOLAOU, P.N. & LIST, E.J. 1988 Investigations of round vertical turbulent buoyant jets. *J. Fluid Mech.* **195**, 341–391.

PHAM, M.V., PLOURDE, F. & DOAN, K.S. 2007 Direct and large-eddy simulations of a pure thermal plume. *Phys. Fluids* **19** (12), 125103.

PITTS, W.M. 1986 Effects of global density and Reynolds number variations on mixing in turbulent, axisymmetric jets. *Tech. Rep.* NIST Publications NBSIR 86-3340.

PITTS, W.M. 1991*a* Effects of global density ratio on the centerline mixing behavior of axisymmetric turbulent jets. *Exp. Fluids* **11**, 125–134.

PITTS, W.M. 1991*b* Reynolds number effects on the mixing behavior of axisymmetric turbulent jets. *Exp. Fluids* **11**, 135–141.

RAYLEIGH, LORD 1882 Investigation of the character of the equilibrium of an incompressible heavy fluid of variable density. *Proc. Lond. Math. Soc.* **s1-14** (1), 170–177.

VAN REEUWIJK, M. & CRASKE, J. 2015 Energy-consistent entrainment relations for jets and plumes. *J. Fluid Mech.* **782**, 333–355.

RICHTMYER, R.D. 1960 Taylor instability in shock acceleration of compressible fluids. *Commun. Pure Appl. Maths* **13** (2), 297–319.

SHABBIR, A. & GEORGE, W.K. 1994 Experiments on a round turbulent buoyant plume. *J. Fluid Mech.* **275**, 1–32.

SKAMAROCK, W.C., PARK, S.-H., KLEMP, J.B. & SNYDER, C. 2014 Atmospheric kinetic energy spectra from global high-resolution nonhydrostatic simulations. *J. Atmos. Sci.* **71** (11), 4369–4381.

TAHA, M., ZHAO, S., LAMORLETTE, A., CONSALVI, J.L. & BOIVIN, P. 2022 Lattice-Boltzmann modeling of buoyancy-driven turbulent flows. *Phys. Fluids* **34** (5), 055131.

TALBOT, C., AFTABI, P. & CHEMIA, Z. 2009 Potash in a salt mushroom at Hormoz Island, Hormoz Strait, Iran. *Ore Geol. Rev.* **35** (3), 317–332.

TAYLOR, G.I. 1950 The instability of liquid surfaces when accelerated in a direction perpendicular to their planes. I. *Proc. R. Soc. Lond.* A **201** (1065), 192–196.

WAITE, M.L. 2011 Stratified turbulence at the buoyancy scale. *Phys. Fluids* **23** (6), 066602.

WANG, H. & LAW, A.W.-K. 2002 Second-order integral model for a round turbulent buoyant jet. *J. Fluid Mech.* **459**, 397–428.

WUNSCH, C. 2002 What is the thermohaline circulation? *Science* **298** (5596), 1179–1181.

WUNSCH, C. & FERRARI, R. 2004 Vertical mixing, energy, and the general circulation of the oceans. *Annu. Rev. Fluid Mech.* **36** (1), 281–314.

WYNGAARD, J.C. & COTÉ, O.R. 1971 The budgets of turbulent kinetic energy and temperature variance in the atmospheric surface layer. *J. Atmos. Sci.* **28** (2), 190–201.

YAN, Z.H. 2007 Large eddy simulations of a turbulent thermal plume. *Heat Mass Transf.* **43** (6), 503–514.